Local distortions and metal-semiconductor-metal transition in quasi-one-dimensional nanowire compounds $AV_3Q_3O_\delta$ (A=K, Rb, Cs and Q=Se, Te)

Zhongnan Guo,^{a,b,∇} Fan Sun,^{a,∇} Danilo Puggioni,^c Yubo Luo,^b Xiaotong Li,^b Xiuquan Zhou,^d Duck Young Chung,^d Erjian Cheng,^e Shiyan Li,^e James M. Rondinelli,^c Wenxia Yuan,^{*a} and Mercouri G. Kanatzidis^{*b,d}

- ^a Department of Chemistry, School of Chemistry and Biological Engineering, University of Science and Technology Beijing, Beijing 100083, China
- ^b Department of Chemistry, Northwestern University, Evanston, Illinois 60208, United States
- ^c Department of Materials Science and Engineering, Northwestern University, Evanston, Illinois 60208, United States
- ^d Materials Science Division, Argonne National Laboratory, Lemont, Illinois 60439, United
 States
- ^e State Key Laboratory of Surface Physics, Department of Physics and Laboratory of Advanced
 Materials, Fudan University, Shanghai 200433, China

Abstract

Metal cluster compounds have garnered renewed interest in the search for novel superconductors and topological semimetals owing to structural instabilities of metal-cluster geometries and broken symmetries. Here we synthesized needle-like crystals of the V-cluster-based quasi-one dimensional (Q1D) materials $AV_3Q_3O_\delta$ (A = K, Rb, Cs, Q = Se, Te) which can also be viewed as being composed of parallel nanowires. We examine how changes in their average and local structure control their electronic properties. All compounds crystallize in the $TlFe_3Te_3$ -type structure ($P6_3/m$ space group) with infinite (V_3Q_3)⁻ double-walled columnar chains separated by A^+ cations. Our single-crystal and synchrotron powder diffraction studies indicate oxygen atoms partially occupy the center site of the V_6 octahedral metal cluster cages in $KV_3Te_3O_{0.33}$, $RbV_3Te_3O_{0.32}$, and $CsV_3Te_3O_{0.35}$, whereas KV_3Se_3 is structurally oxygen-free. Our synchrotron

X-ray pair distribution function (PDF) analyses indicate that the oxygen-free V₆ cluster octahedra in KV₃Se₃ are highly distorted perpendicular to the chain direction even at room temperature, reducing the symmetry of the average structure from hexagonal P6₃/m to monoclinic P2₁/m. Our theoretical calculation supports this P2₁/m distortion and suggests the structure further distorts to P2₁ or P2₁/c at lower temperatures. In contrast, the oxygen-centered V-cluster in KV₃Te₃O_{0.33} exhibits a V₃-triangle-trimerization along the chain direction. This feature is discernable from the local PDF and is consistent with lattice dynamical calculations based on density functional theory. Resistivity measurements indicate that KV₃Se₃ exhibits metallic behavior, whereas a dramatic metal-semiconductor-metal transition emerges in KV₃Te₃O_{0.33}, RbV₃Te₃O_{0.32}, and CsV₃Te₃O_{0.35} because of oxygen disorder and changes in local structure captured from our electronic structure analyses of the Fermi surface. Our investigation of the AV₃Q₃O₆ family demonstrates the importance of understanding local changes in structure driven by electronic instabilities, which can guide the search for new quantum materials in other low-dimensional cluster-compound materials.

Introduction

Quasi-one dimensional (Q1D) subvalent materials (or metal-rich compounds) are of interest to both chemists and physicists owing to their rich structural chemistry and collective phenomena they may exhibit. [1-3] These compounds generally contain extensive metal-metal bonds. forming diverse Q1D clusters about the metal lattice (Figure 1). The resultant non-integer or low metal oxidation states, combined with the low dimensionality typically expressed as perfectly defined molecular nanowires, often lead to exotic physical properties such as unconventional superconductivity [4][5] and a charge-density-wave state. [6] Nb₃Q₄ (Q = S, Se, Te) exhibit a hexagonal space group with parallel zigzag Nb chains along the c direction and are all superconductors (at 4.0, 2.0 and 1.8 K, respectively). [5][7] Orthorhombic BaFe₂S₃ exhibits a two-leg ladder Fe configuration and is a Mott insulator with stripe-type antiferromagnetic order and moments along the rung direction at ambient pressure. [8] It transforms into a superconducting state at 24 K under 11 GPa. [9][10] Hexagonal AMo₃Q₃ (A = K, Rb, Cs, Tl, In and Q=Se, Te) contain face-sharing Mo₆ octahedral clusters surrounded by Q atomic tubes, which are structurally related to the building blocks comprising Chevrel phases. [11][12] In this family, A = Tl and In are metallic and become superconducting below 5 K, whereas A = K and Rb are semiconducting at low temperature as a consequence of a fluctuating Peierls gap. [13][14] Ta₄ZTe₄ (Z=Si, Cr, Fe, Co, Ni), crystallizing as nanowires in the orthorhombic crystal system, are constructed from Z-centered Ta₈ square antiprisms with common square faces. [15][16] Last, monoclinic KMn₆Bi₅ contains Mn-centered pentagonal clusters of Mn₁₀ antiprisms fused to form unique nanowires, [17] and it shows unusual microstructures with stress-induced domain structures and anisotropic physical properties.^[18]

Recently, cluster compounds have undergone a revival as the related lower-dimensional chalcogenides can exhibit topological electronic band structure features. ^[19] Considering that having one electron per atomic orbital is either chemically unstable or highly localized, one can use one electron per molecular orbital in cluster compounds instead, to induce the band crossing near Fermi level and achieve the Dirac or Weyl semimetal state. ^[19] These semimetallic states are also supported by the lower effective dimensionality and the capability to control crystallographic symmetry by changes in composition in metal-cluster compounds. Indeed, the 2D ZrSiS with a silicon square net ^{[20][21]} and the 3D Ir₂In₈Q (Q=S, Se, Te) with IrIn₈ bicapped trigonal prism cluster ^{[22][23]} are experimentally confirmed to be topological semimetals.

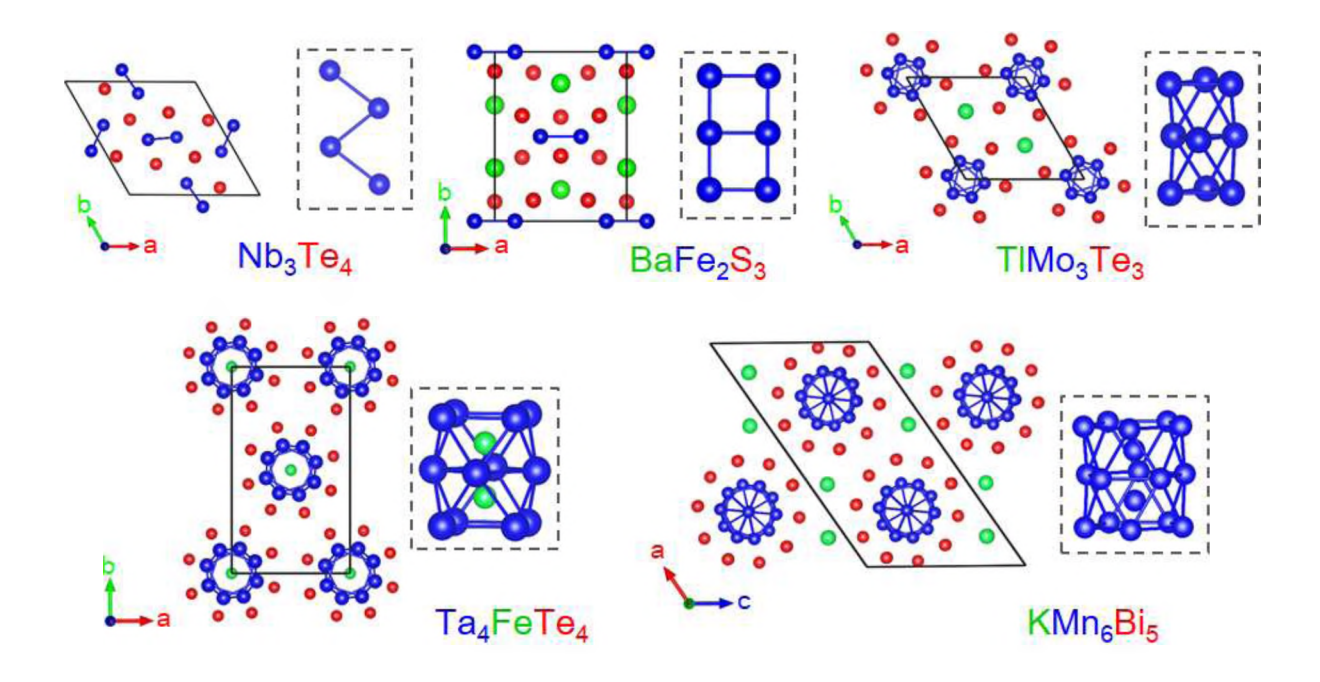


Figure 1. Crystal structure of some reported Q1D metal cluster compounds: hexagonal Nb₃Te₄, orthorhombic BaFe₂S₃, hexagonal TlMo₃Te₃, orthorhombic Ta₄FeTe₄ and monoclinic KMn₆Bi₅. Details of the Q1D metal clusters (shown in blue colour) for each material along the chain direction are shown in the dotted box: Nb zigzag chain, Fe biatomic chain, Mo face-shared octahedra, Ta square antiprism, and Mn pentagon antiprism.

Among the metal-cluster compounds, Q1D face-sharing octahedral cluster materials in TlFe₃Te₃-structure type (*P*6₃/*m* symmetry) are also viable topological semimetal candidates. High-resolution angle-resolved photoemission spectroscopy showed a Dirac-like energy band near the Fermi surface of TlMo₃Se₃.^[24] Furthermore, theoretical models proposed that the TlFe₃Te₃-structure type could host cubic Dirac fermions based on the nonsymmorphic symmetry originating from the 6₃-screw axis.^{[19][25][26]} These interesting TlFe₃Te₃-type phases, however, are currently limited to transition metals of Fe, Mo, Cr, and Ni,^[11, 27-30] and extending them to other chemistries would enable access to additional band fillings and magnetic states.

Beyond searching for topological excitations, finding superconductivity in materials with strong electron-electron interactions led to the discovery of $A_2Cr_3As_3$ (A = K, Rb, Cs) with Q1D face-sharing Cr_6 octahedral chains. These materials are structurally similar to the aforementioned AMo_3Q_3 compounds, but exhibit twice as many alkali metals to maintain similar electron filling upon replacing Q with the arsenide ions. [30-32] Taddei et al., reported a structural instability in the

Cr triangle plane at low temperature, leading to local distortions and accordingly unconventional superconductivity in A₂Cr₃As₃.^[33] The derivative family with a single alkali metal, ACr₃As₃ (A = K, Rb, Cs), adopt the same *P*6₃/*m* symmetry as the AMo₃Q₃ chalcogenides and were initially reported to exhibit a nonsuperconducting spin-glass ground state.^{[34][35]} Very recently, however, hydrogen occupancy at the center of Cr₆ octahedra in ACr₃As₃ was reported. Upon increasing the H concentration, the Cr₆ octahedral distortion can be controlled and superconductivity induced, demonstrating a strong interplay among the Q1D cluster geometry, band filling, and magnetism that requires deeper understanding for further property control. ^[36-39]

Although the Q1D telluride $KV_3Te_3O_{0.42}$ adopts the same $P6_3/m$ symmetry as the Moand Cr-based compounds, it contains V₃ cluster triangles stacked side-by-side into columnar chains with oxygen unexpectedly occupying the center of the octahedra as discerned from single crystal X-ray diffraction. [40] Here we report single-crystal synthesis employing an A₂Q_x flux of a series of Q1D V-based TlFe₃Te₃-type crystals: KV₃Se₃, KV₃Te₃O_{0.33}, RbV₃Te₃O_{0.32}, and CsV₃Te₃O_{0.35}. Single-crystal and synchrotron powder X-ray diffraction indicate the occupation of oxygen at the center of the V₆ octahedral cluster formed by two V₃ clusters for three tellurides, while the selenide KV₃Se₃ is structurally oxygen-free. Based on density functional theory (DFT) calculations and pair distribution function (PDF) analyses, we find that a strong local distortion, perpendicular to the column direction, occurs in KV₃Se₃ even at room temperature, lowering the average structure symmetry from $P6_3/m$ to $P2_1/m$. This in-plane octahedral distortion is suppressed by the centered oxygen in isostructural KV₃Te₃O_{0.33}, but KV₃Te₃O_{0.33} shows a different out-of-plane V₃-triangle-trimerization along the chain direction to form V₉ clusters with the oxygen atoms locating between the clusters. Variable temperature PDF analysis also indicates that these local distortions occur over a wide temperature range from 87 to 400 K. Resistivity measurements on AV₃Te₃O_δ show a dramatic metal-semiconductor-metal transition, which we attribute to oxygen disorder and a potential Lifshitz-like transition. Our results highlight how complex structural distortions and electronic transitions can arise in Q1D cluster compounds by controlling electron count in cluster-centered anions, providing a unique platform to search for novel quantum properties.

Results and Discussion

Crystal growth and average structure

Crystal growths were carried out using A_2Q_x flux with the molar ratio A:V:Te = 7:3:12 for AV₃Te₃O_{δ} (A = K, Rb, Cs) and K:V:Se = 7:3:7 for KV₃Se₃, as described in the Experiment section. The A_2Q_x flux can enhance atomic diffusion during synthesis and facilitate large crystals. Very thin black needle-like crystals mainly in 3-4 mm length were harvested, exhibiting typical hexagonal prism morphology, see Figure 2a. The crystals are malleable and remain stable in air and water (Figure S1, Supporting Information). Composition analyses of these compounds were done on the fresh crystal surface using X-ray analysis with energy dispersive spectroscopy (EDS). The results are close to the stoichiometric 1:3:3 ratio. Elemental mapping of KV₃Se₃ confirms the presence of K, V, and Se in KV₃Se₃, which are homogeneously distributed (Figure S2). We found that the chalcogen ratio required to grow KV₃Se₃ (7:3:7) was much less than that for AV₃Te₃O_{δ} (7:3:12), likely owing to the larger electronegativity of selenium. Increasing the Se content to 7:3:9 or decreasing V to 7:2:7 led to the formation of VSe₂ plate-like crystals identified by EDS.

As grown needle-like crystals with dimensions $0.1 \times 0.1 \times 1 \text{ mm}^3$ were selected for single X-ray diffraction and they were not acquired as fragments of larger crystals. All the compounds adopt the TIFe₃Te₃-type structure with the $P6_3/m$ space group (No. 176) composed of infinite $[V_3Te_3]^-$ or $[V_3Se_3]^-$ columnar chains along the c axis (or [001] direction) with the alkali metal ions filling the space between the chains (Figure 2b, c). The V-cluster chains comprise stacked V_3 cluster triangles where each triangle is rotated by 60 degrees with respect to its neighbor. This is the same structural configuration as in the Mo- and Cr-based compounds. [11][34] The V_3 triangles exhibit the same V-V bond distances in the ab plane (V- $V_{in-plane}$) and are structurally related by a crystallographic 6_3 screw axis (C_6 rotation axis) along c (Figure 2d). The in-plane V-V bond lengths (~2.7 to 2.8 Å) are slightly larger than that in elemental V (~2.62 Å), but are shorter than twice the covalent radius of V signifying metallic bond formation within the chains. The V-V bond distance between different triangle planes (V- $V_{out-of-plane}$), ranges from ~2.68 to 2.77 Å, and it is shorter than that of V- $V_{in-plane}$, leading to compressed octahedra along the chain direction.

In addition, each V center is coordinated to four chalcogen anions, Figure 2e. The chalcogen anions surround the V_3 cluster-based columns, forming a nanotube that acts as the cladding for the metallic chains. Thus, it exhibits a double-walled $(V_3Q_3)^-$ nanowire motif. The intrachain $Q\cdots Q$ distances are ~ 3.66 Å for KV_3Se_3 and ~ 3.94 Å for the three tellurides, indicating non-

bonding interactions inside the nanowires. The alkali metal A^+ ions are coordinated to nine chalcogen anions in the shape of a tricapped trigonal prism and these prisms share triangular faces along c direction (Figure 2f). The crystallographic information is listed in Table S1-12 in the Supporting Information.

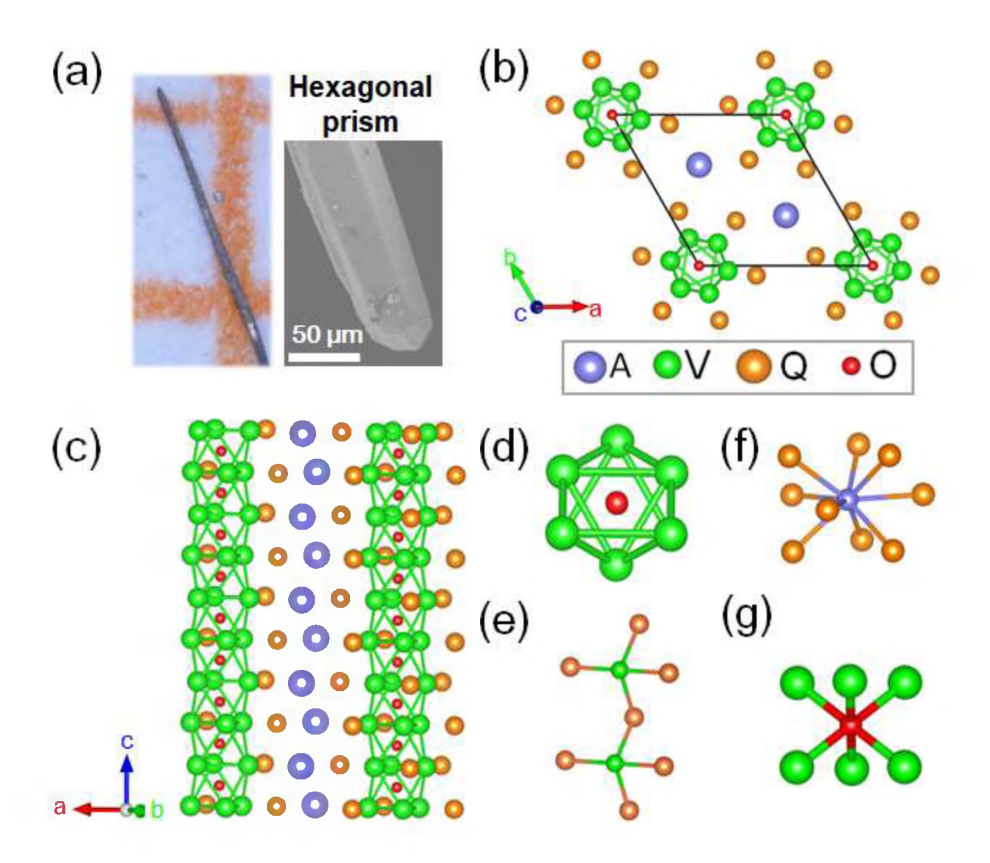


Figure 2. (a) Optical photograph and scanning electron microscopy image of KV_3Se_3 crystals, showing the cagonal prism nature. (b) Crystal structure of $AV_3Q_3O_\delta$ (A = K, Rb, Cs and Q = Se, Te) viewed along the chain direction [001]. (c) Side view of the structure perpendicular to the chain direction. (d) Enlarged V_6 octahedron showing ideal V_3 triangle. The chemical coordination of (e) V, (f) alkali metal A, and (g) oxygen atom.

Based on single crystal X-ray diffraction (SCXRD), we observed interstitial oxygen atoms at the center of the V₆ cluster octahedra in all telluride crystals (Figure 2d and 2g). The electron density map of KV₃Te₃ shows that the highest residual peak of ~7.27 e Å⁻³ is located at the center of V octahedron and this residual density also occurs for the other two tellurides (~7.27 e Å⁻³ for Rb V₃Te₃ and ~7.7 e Å⁻³ for CsV₃Te₃) (Figure S3). After modeling these residual peaks by O atoms, the refinements also significantly improved with low values of weighted agreement factors (Supporting Information), indicating good structure solution. Based on the refined occupa-

tion, we deduced the chemical formula for the three tellurides as $KV_3Te_3O_{0.33}$, $RbV_3Te_3O_{0.32}$ and $CsV_3Te_3O_{0.35}$. We speculate that the oxygen comes from the oxidized surface of our raw materials (the vanadium powders and/or alkali metals), which is supported by the powder X-ray diffraction of our polycrystalline sample presented below. Note this centered oxygen atom was also observed by Wu et al., in $KV_3Te_3O_{0.42}$, where the O content, 0.42, is larger than our results. [40] We note that the presence of interstitial oxygen in $AV_3Te_3O_6$ is an unintentional effect and was not part of our synthetic aim. Using current raw material purity and our synthetic route, three telluride crystals from many different batches always exhibited oxygen in structure, although we did not add any oxide as starting materials during synthesis. In contrast, no residual peak was located at the center of the V_6 cluster octahedra for KV_3Se_3 , indicating an oxygen-free compound. Diffraction measurements were carried out on another KV_3Se_3 crystal from a different batch and the density peak at the center of octahedron was still absent. Hence, we conclude that despite being isostructural with $AV_3Te_3O_6$, KV_3Se_3 is completely oxygen-free, exhibiting "empty" V_6 cluster octahedra.

To confirm this chalcogenide-dependent O interstitial occupancy, we performed synchrotron powder X-ray diffraction (SPXRD) on our polycrystalline samples (See Experiment section for a description of the synthesis). Figure 3 shows the high-resolution SPXRD patterns for polycrystalline KV_3Se_3 and $KV_3Te_3O_\delta$ samples collected at room temperature. All patterns were indexed to a hexagonal cell with space group $P6_3/m$. The SCXRD structures were used as initial models to refine the SPXRD patterns and show good fits (Table S13 and S14), indicating correct structure solutions obtained from our SCXRD analyses. Negligible secondary phases were present in the $KV_3Te_3O_\delta$ SPXRD pattern, however, adding centered oxygen in the V_6 cluster octahedra improved the refinement. We refined the O occupancy to 0.14(1), which is less than what we obtained from the SCXRD. As expected, following a similar refinement procedure for the SPXRD pattern of KV_3Se_3 led to no interstitial oxygen, consistent with the SCXRD result.

Unlike the high phase purity observed for the $KV_3Te_3O_\delta$ powders, impurity reflections were clearly discernible in the KV_3Se_3 SPXRD pattern, which we identified as the oxyselenide KV_2Se_2O (~9.3 at.%), a new compound isostructural with the reported oxytellurides RbV_2Te_2O and CsV_2S_2O (Figure S4). [41][42] Therefore, we suggest that the origin of oxygen during the synthesis was from the oxide impurity in our starting materials. When growing KV_3Se_3 single crystals, the oxide impurity was removed together with the K_2Se_x flux by centrifugation. In contrast,

the tellurides need to incorporate the oxygen at the center of V_6 cluster octahedra to stabilize the structure, so the oxygen was involved to form the $AV_3Te_3O_\delta$ phases (details will be discussed in the Theoretical electronic structures section).

Figure 4 shows the lattice parameters, $Q \cdots Q$ distances, and V-V bond lengths based on the SCXRD refinements. The a lattice parameter of $AV_3Te_3O_\delta$ increases nearly linearly (~0.5 Å) with increasing size of the A^+ ion, expanding the basal plane of the hexagonal cell. In contrast, there is no monotonic increase for the c parameter, which is geometrically equal to twice the distance between two V triangle planes. The c lattice parameter only changes in the ~0.02 Å range, achieving a maximum value for the Rb analogue, Figure 4b. The $Q \cdots Q$ distances and V-V bond lengths exhibit similar dependencies as the c lattice parameter, i.e., they are independent of the radius of the alkali metal ion (Figure 4c, d and e). Similar trends were observed in ACr_3As_3 and ANi_3Se_3 systems, [29][35] indicating that the double-walled chain in the Q1D face-sharing octahedral structure is basically unaffected by the radius of the A^+ ions.

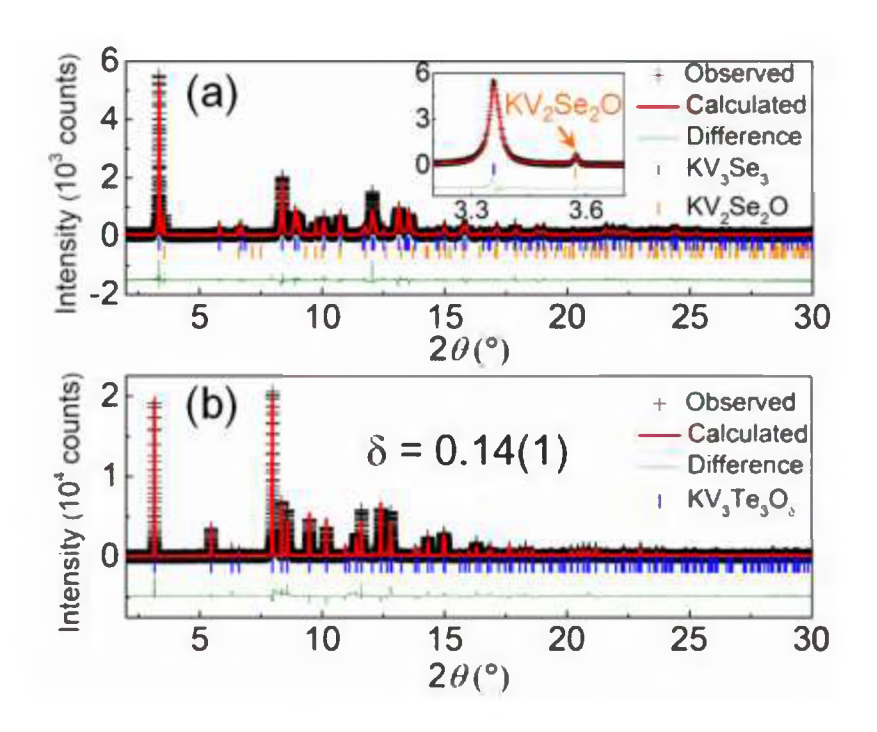


Figure 3. Synchrotron PXRD patterns for (a) KV_3Se_3 and (b) $KV_3Te_3O_8$ polycrystalline samples. Inset of (a) shows the enlarged part in the low 2θ range, clearly showing the presence of KV_2Se_2O impurity (~9.3 at.%).

The lattice parameters of KV₃Se₃ are significantly shorter than that of tellurides because of the smaller radius of Se²⁻ compared to Te²⁻. In KV₃Se₃ the V-V metallic bonds are shortened by ~0.1 Å compared with that in KV₃Te₃O_{0.33} (Figure 4d and 4e). This behavior is different from the AMo₃Q₃ system where the Mo-Mo bond distances are basically the same in KMo₃Se₃ and KMo₃Te₃. This discrepancy also strongly supports the structure refinement above that the KV₃Te₃O_{0.33} contains centered oxygen atoms in the V₆ cluster octahedra whereas KV₃Se₃ does not. Interestingly, we obtained large error bars for the V-V bond lengths in all materials, but especially in KV₃Se₃ (Figure 4d, e), which results from the large V anisotropic displacement parameters (ADPs) in the *ab* plane (U₁₁ and U₂₂, see Table S3). Generally, large ADP values are indicative of local lattice distortions that may be of lower symmetry than the average structure. Here, the large ADPs in KV₃Se₃ suggest the V triangles are not equilateral but rather distorted in a manner to lower the macroscopic *P*6₃/*m* symmetry.

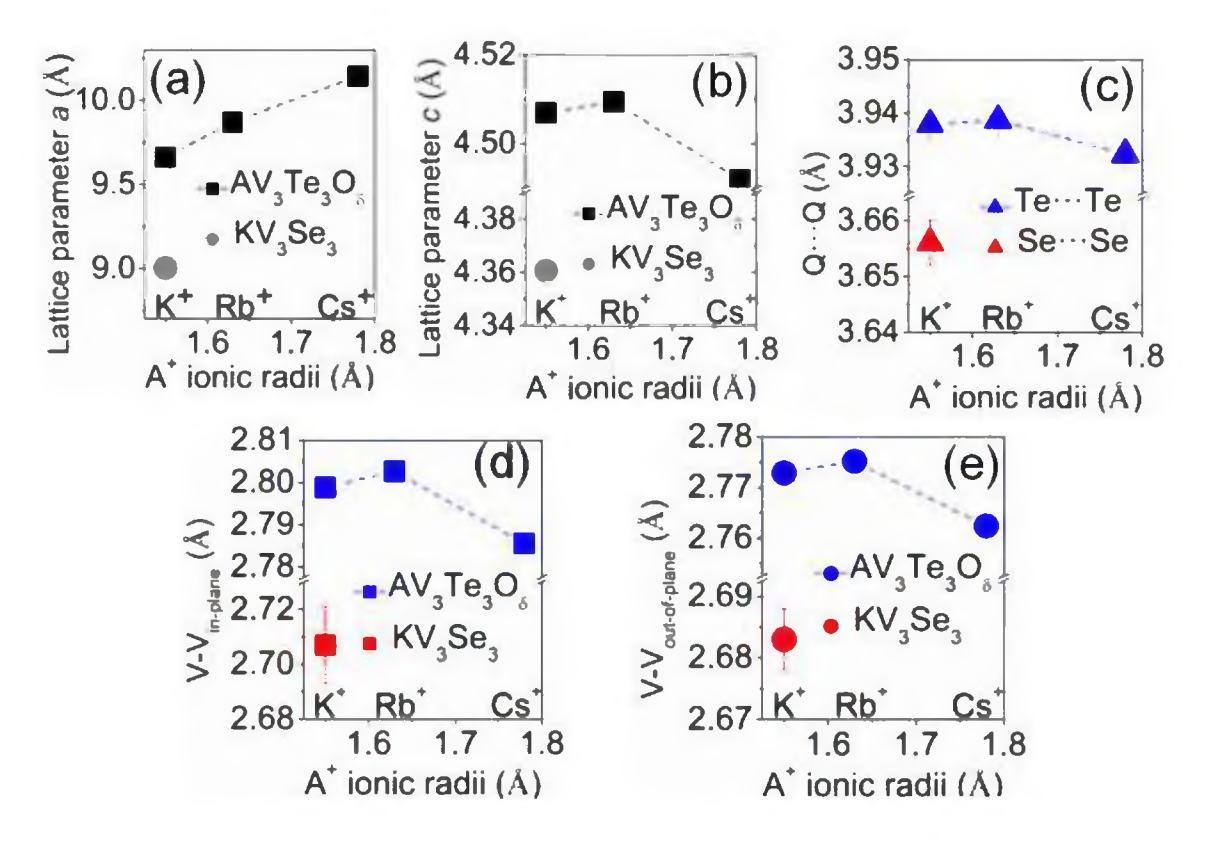


Figure 4. The structural parameters of $AV_3Te_3O_\delta$ obtained from single-crystal X-ray diffraction: (a) a, (b) c, (c) $Q\cdots Q$ distance, (d) $V-V_{in-plane}$ bond length, and (e) $V-V_{out-of-plane}$ bond length.

Local structure of KV₃Se₃

To examine possible local structural distortions in KV₃Se₃, we performed density functional theory (DFT) calculations to relax the internal coordinates of the hexagonal $P6_3/m$ phase using the lattice parameters from our SCXRD (see Methods for details). After energy minimization, we found that the $P6_3/m$ symmetry transforms spontaneously into a structure with $P2_1/m$ monoclinic symmetry (Figure 5a). In the $P2_1/m$ symmetry, the formerly single V Wyckoff site splits into three sites thereby permitting different V-V bond lengths in the ab plane. This distortion lifts the C_6 symmetry and transforms the C_6 screw axis into a C_6 screw axis. The energy gain from the distortion is as large as C_6 eV per formula unit (f.u.), which is well-beyond the error for DFT calculations, suggesting the strong dynamical instability of the C_6 m phase at zero Kelvin.

Both room-temperature single-crystal and powder X-ray diffraction data support the assignment of $P6_3/m$ symmetry, indicating that this instability identified from DFT may either coherently occur at lower temperatures, i.e., resulting in a phase transition, and/or may appear at room temperature in the form of local displacements away from $P6_3/m$ symmetry towards $P2_1/m$. To that end, we probed the existence of local distortion not captured by the average structure determind by the single crystal X-ray diffraction analysis, using atomic pair distribution function (PDF) analyses of synchrotron X-ray total scattering. These data were collected on polycrystalline samples of the V-based Q1D compounds to examine the local structure. We firstly extracted G(r) functions collected at 300 K and fitted the data using the symmetry constraints of $P6_3/m$ and $P2_1/m$, respectively, focusing on the low-r region spanning 2.2-5.9 Å which covers only one $(V_3Se_3)^-$ double-walled chain in the ab plane to accentuate the local structure. The $P6_3/m$ model is inconsistent with the experimental PDF data as demonstrated by the relatively high value of the weighted agreement factor, $R_w = 19.9\%$ (Figure S5). Even upon including KV₃Se₃O as a secondary phase for the fit, we found the $P6_3/m$ model remained poor (Figure S6 and details in the SI); hence, we processed all PDF data on KV₃Se₃ using a single-phase model. In contrast, refinement based on the DFT-predicted $P2_1/m$ model led to a considerably improved fit to the experimental PDF data for KV_3Se_3 ($R_w = 6.5\%$).

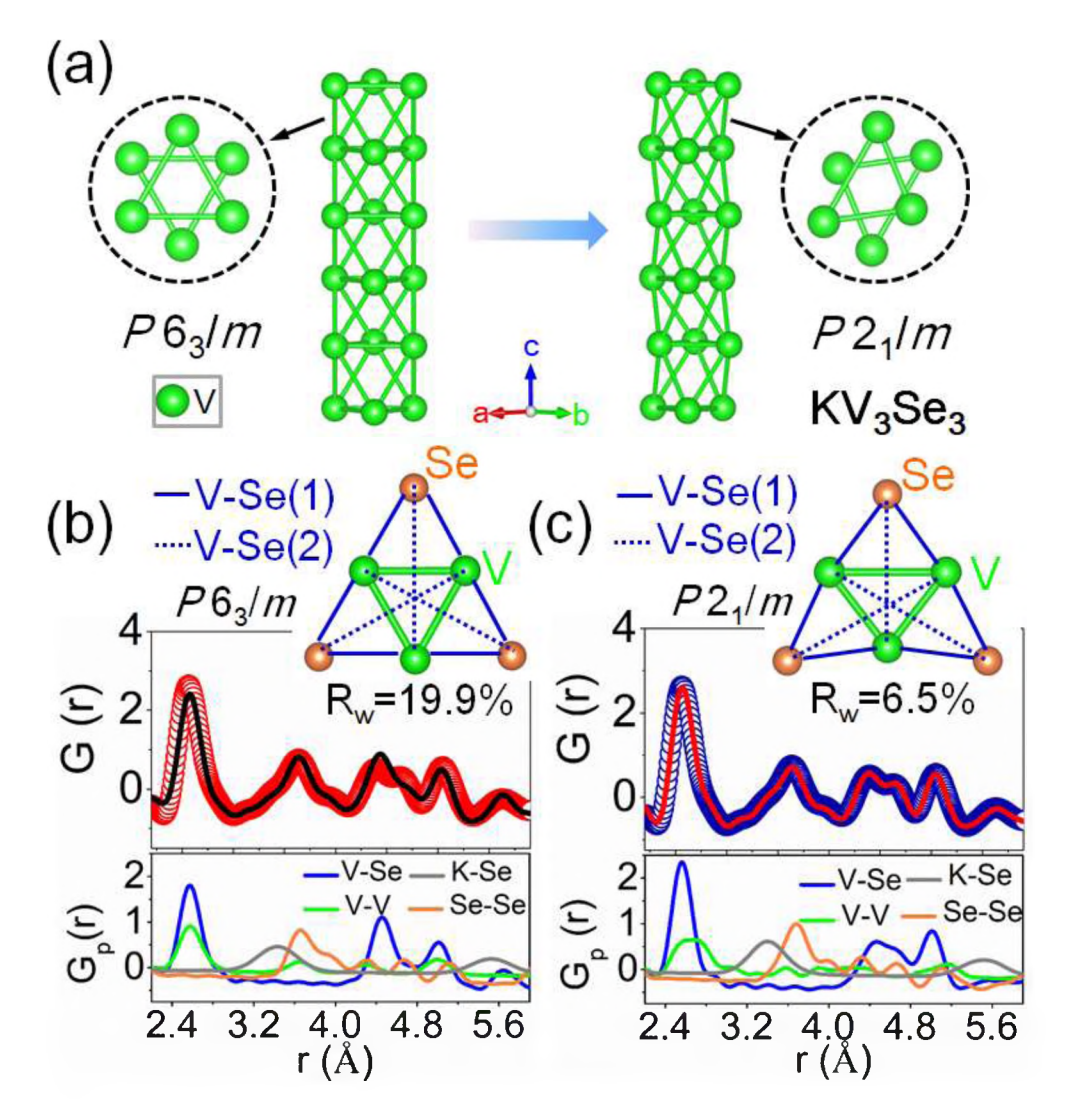


Figure 5. Analysis of local distortions in KV_3Se_3 . (a) The structural distortion predicted by the DFT calculations comprises V displacements in the *ab* plane, which lift the C_6 symmetry and reduce the space group from $P6_3/m$ to $P2_1/m$. PDF fits for KV_3Se_3 with the (b) $P6_3/m$ model and the (c) $P2_1/m$ model over the low r range (2.2-5.9 Å) at 300 K. The calculated partial PDFs, $G_p(r)$, obtained for the V-Se, V-V, Se-Se and K-Se correlation functions are also shown. The red and blue circles correspond to the experimental data. The black and red lines represent the calculated data based on the structural models. The partial PDF peaks labeled by V-Se(1) and V-Se(2) correspond to the nearest and next nearest V-Se atom pairs, depicted in the top right of panels of (b) and (c). It should be mentioned that although the V-Se(1) pairs include V-Se distances between two adjacent $(V_3Se_3)^r$ layers, only contributions from a single layer are shown here for clarity.

The residuals that produce the high R_w in the $P6_3/m$ model are mainly due to poor fitting of the ~4.5 Å peak, where significant peak splitting occurs in the experimental data (Figure 5b). The in-plane ADP of V obtained with the $P6_3/m$ model are also large (~0.0304 Å²), consistent

with the SCXRD refinement. Next, we plotted the PDF fit in the low-r region together with the partial PDF simulation, to identify the atomic pairs contributing to each PDF peaks (Figure 5b, c lower panels). We find the first PDF peak at ~2.5 Å is due to nearest-neighbor V-Se pairs, denoted as V-Se(1), and the V-V metallic bonds. Here, there is a clear shoulder on the right side of this peak in the PDF data and the large in-plane V ADP values in the P6₃/m model result from attempting to fit this shoulder. However, the split PDF peak at ~4.5 Å, which is due to the next-nearest neighbor V-Se pairs (denoted as V-Se(2)), is still poorly described. The split peak at ~4.5 Å was not due to the KV₂Se₂O impurity (see Figure S6) and hence attributed to an intrinsic structural distortion in KV₃Se₃.

Based on our models, we find different V-Se(2) pair distances are required to capture the split PDF peak at ~4.5 Å. By removing the symmetry constraints imposed by the $P6_3/m$ symmetry, i.e., distorting the V equilateral triangle into non-equilateral, into the $P2_1/m$ symmetry identified from our DFT calculations, the G(r) functions for the V-V pairs significantly broaden to improve the fit of the shoulder located beside the first PDF peak near ~2.5 Å. More importantly, this in-plane distortion permits very different V-Se(2) distances (Figure 5c, inset), allowing the $P2_1/m$ structure model to capture the ~4.5 Å peak splitting and reduce the R_w . The in-plane ADP also decreases to 0.0062 Å² in the $P2_1/m$ model.

Importantly, refinement of the experimental PDF of KV₃Se₃ over the high-r range from 15 to 30 Å shows that the $P6_3/m$ model outperforms the $P2_1/m$ one (Figure S5). This indicates that the local distortions of the V triangle in each single (V₃Se₃)⁻ tube (as r < 6 Å) are uncorrelated beyond this length scale, hence leading to an average long-range structure of $P6_3/m$ in KV₃Se₃ and its large SCXRD observed in-plane V ADPs. Usually such distortions cooperatively order at low temperature, provided the interactions driving the local distortion are sufficiently long range, and KV₃Se₃ should exhibit a phase transition. Based on our PDF refinement, the cluster columns in KV₃Se₃ remain highly distorted in the ab plane even at room temperature and its persists from 400 K down to 87 K without an obvious phase transition into the ordered $P2_1/m$ structure (see Figure S7 and S8). Upon further examination of the zero Kelvin dynamical stability of the monoclinic $P2_1/m$ phases (Figure S9a), we found additional displacive instabilities in the Brillouin zone indicating the local ab plane distortions and long-range order afforded by the $P2_1/m$ average structure is one among several low energy configurations for the (V₃Se₃)⁻ tubes. To that end, we

searched for competing phases by systematically imposing linear combinations of the phonon eigen-displacements corresponding to the two most unstable modes, which are located at Γ and B (Figure S9a), and performing structural optimization on these candidate low-symmetry structures. Our calculations suggest that at low temperature the $P2_1/m$ structure can transform to either the monoclinic $P2_1/c$ polymorph or the polar $P2_1$ polymorph. Although the energy difference between these two structures is only 0.2 meV/f.u. in favor of the nonpolar $P2_1/c$ structure, which make them essentially degenerate, both phases are approximately 6 meV/f.u. lower in energy than the $P2_1/m$ phase (Figure S9b). The distortion vectors relative to the $P2_1/m$ phase correspond to irreducible representations B_1^- and Γ_1^- for the polar and nonpolar structures, respectively. Importantly, there is no group-subgroup relation between the $P2_1/c$ polymorph (described by four formula units) and the $P2_1$ polymorph (2 formula units) (Figure S9c).

Our calculations suggest KV₃Se₃ should exhibit a phase transition from $P2_1/m$ to $P2_1/c$ (or $P2_1$) at low temperature, corresponding to approximately 70 K based on total energy differences. To check this low temperature phase transition, we tried to fit the PDF data at 87 K (the limit of the beam line we used) using four models, $P6_3/m$, $P2_1/m$, $P2_1/c$ and $P2_1$. As shown in Figure S10, the $P2_1/m$ structure model significantly improves the fit compared with the $P6_3/m$ phase. The $P2_1/c$ and $P2_1$ models also show high goodness of fit, but they do not outperform the $P2_1/m$ structural model, indicating the local structural distortions are dominated by those in the $P2_1/m$ model. Future lower temperature PDF measurements should be performed to search for these possible coherent structural transitions.

Local structure of KV₃Te₃O_{0.33}

We also performed DFT calculations to investigate possible distortions in $KV_3Te_3O_{0.33}$. To simulate $KV_3Te_3O_{0.33}$, we constructed a structural model with the ordered oxygen atoms such that the centered oxygen atoms occupy one in every three V_6 cluster octahedra. The simulation cell thus comprises a unit cell with a three times larger c lattice parameter (Figure 6a). In contrast to the distortion in KV_3Se_3 along the ab plane, the theoretical model of $KV_3Te_3O_{0.33}$ exhibits an out-of-plane structural distortion after the structural optimization, displaying a trimerization along the chain direction, where each V_3 triangle in the ab plane is defined as the monomer,

shown in Figure 6a. The trimerization forms V₉ cluster bi-octahedra without any centered oxygen. And the middle V₃ triangle plane of the trimerization significantly contract compared to the other two V₃ triangles on the edge (Figure 6a, dotted box). Despite the out-of-plane trimerization, all the V₃ triangles remain equilateral without any distortions in the *ab* plane. Thus, the space group remains unchanged within this trimer model, preserving the 6₃-screw axis (Figure 6a, dash circle). The OV₆ octahedron with centered oxygen in KV₃Te₃O_{0.33} is stable after the structural relaxation, suggesting the oxygen atom at the center site plays a key stabilizing role through the formation of V-O bonds (Figure 2g). The dynamical structural stability of the trimer model in Figure 6a is also confirmed by the DFT phonon calculations (Figure S11).

Our PDF analysis shows the trimer model provides a better fit to the experimental data ($R_w = 10.8\%$) than that trimer-free model ($R_w = 14.2\%$) over the low-r range (2.5-6.2 Å), experimentally supporting the DFT identified V₃-triangle-trimerization (Figure S12). The partial PDF simulations shown in Figure 6b and 6c also show the trimer model provides an improved refinement, because of the better fitting of the peak at ~5.3 Å arising from the third nearest neighboring V-Te pairs (V-Te(3)). Refinement with the trimer-free model gives a shorter V-Te(3) pair compared with the experimental data. In contrast, the trimer model compresses the middle V triangle plane in the V₉ cluster and this leads to a longer V-Te(3) distance. However, the distortion is weaker in KV₃Te₃O_{0.33} compared to KV₃Se₃ since the R_w values do not differ significantly between the two models. The reduced distortion is also consistent with the smaller V ADPs obtained from the SCXRD measurements. Similar with KV₃Se₃, refinement on the high-r PDF data from 15 to 30 Å in KV₃Te₃O_{0.33} (Figure S12) indicates that this trimerization is local and no long-range cooperative ordering; however, it persists over the complete temperature range explored, 400 to 87 K, as shown in the temperature-dependent PDF data in Figure S13 and S14.

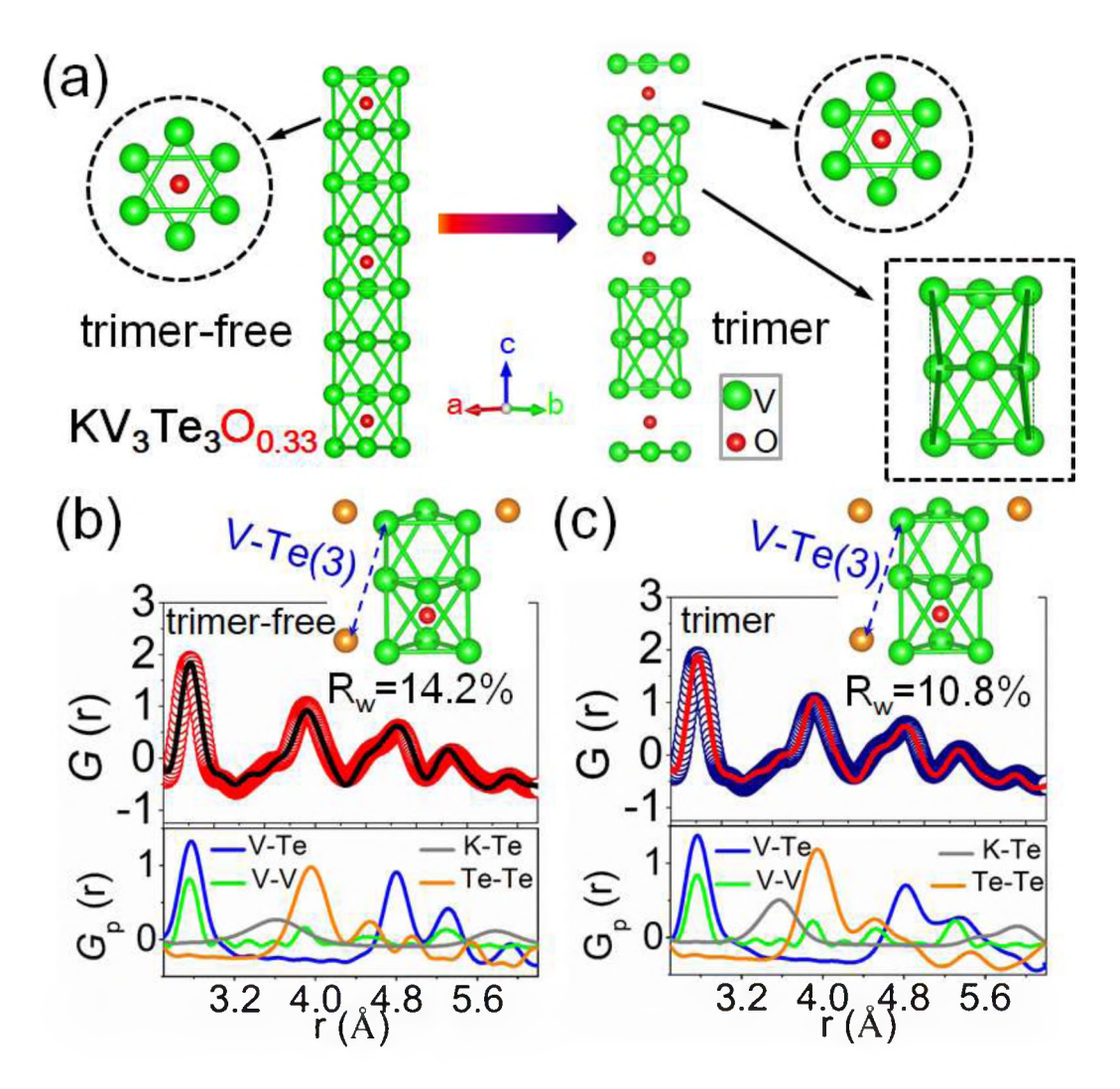


Figure 6. Analysis of local distortions in $KV_3Te_3O_{0.33}$. (a) The structural distortion predicted by the DFT calculations exhibits V_3 -triangel-trimerization along the chain direction. PDF fits for $KV_3Te_3O_{0.33}$ with the (b) trimer-free and (c) trimer model over the low r range (2.5-6.2 Å) at 300 K. The calculated partial PDFs, $G_p(r)$, obtained for the V-Te, V-V, Te-Te and K-Te correlation functions are also shown. The red and blue circles correspond to the experimental data. The black and red lines represent the calculated data based on the structural models. The partial PDF peaks labeled by V-Te(3) correspond to the third nearest V-Te atom pairs, depicted in the top right of panels of (b) and (c).

Physical properties

Figure 7 shows the temperature-dependent resistivity (ρ) of single crystal KV₃Se₃ from 300 to 2 K along the chain direction. KV₃Se₃ displays metallic behavior over the complete tempera-

ture range, and exhibits $\rho = 2.25 \times 10^{-4} \Omega$ cm at 300 K, which is comparable to that of isostructural AMo₃Q₃, ACr₃As₃ and ANi₃Se₃.^{[13][28][34]} Linear behaviour of the resistivity is observed from 300 to 50 K, while a T^2 dependence occurs between 50 and 2 K, which can be fit as $\rho(T) = \rho_0 + AT^2$ with a residual resistivity ρ_0 and constant A of 0.224 × 10⁻⁴ Ω cm and 8.48 × 10⁻⁹ Ω cm/K², respectively, suggesting electron-electron scattering dominates at low temperature.^[43] The residual resistivity ratio (RRR = $\rho(T=300 \text{ K})/\rho(T=2 \text{ K})$) is ~11.3.

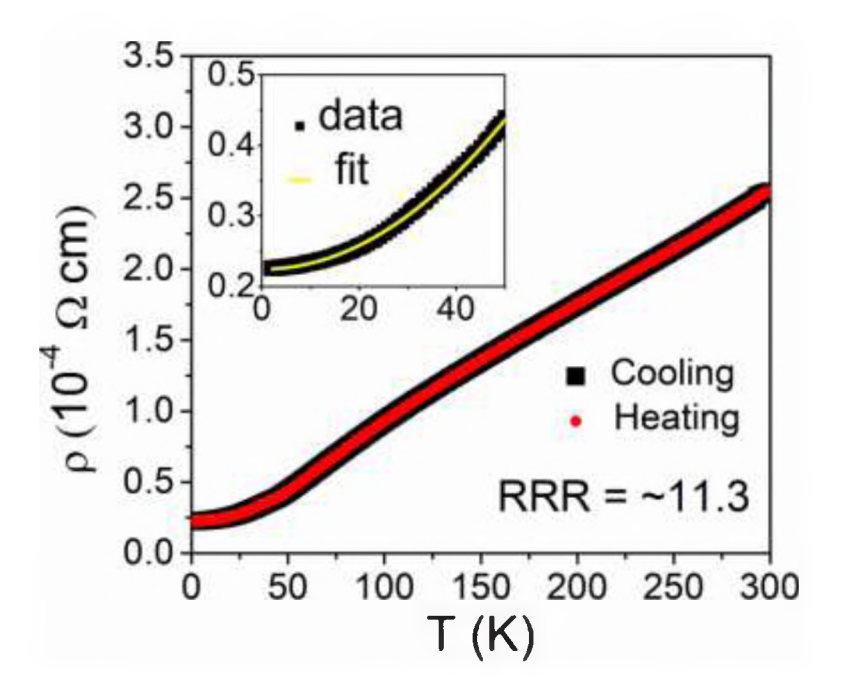


Figure 7. Temperature dependent resistivity of KV₃Se₃ single-crystals from 300 to 2 K. The data at low temperature from 50 to 2 K shown inset follows a $\rho(T) = \rho_0 + AT^2$ dependence.

Figure 8 shows that the temperature-dependent resistivities of AV₃Te₃O₈ exhibit a nontrivial temperature dependence from 300 to 2 K different from that of KV₃Se₃. First, our 300 K resistivities are low, 5.1, 3.8 and $3.8 \times 10^{-4} \Omega$ cm for KV₃Te₃O_{0.33}, RbV₃Te₃O_{0.32} and CsV₃Te₃O_{0.35}, respectively, and are of the same order as KV₃Se₃ and all other TlFe₃Te₃-type compounds (~10⁻⁴ Ω cm). Note that our values are several orders of magnitude smaller than those measured by Wu et al. using a two-probe method on KV₃Te₃O_{0.42} at 298 K (~41.6 Ω cm). Here, all three tellurides exhibit a metal-semiconductor-metal transition identified by the change is sign of $d\rho(T)/dT$. The metal-semiconductor transitions occur at 93 K, 34 K and 95 K for KV₃Te₃O_{0.33}, RbV₃Te₃O_{0.32} and CsV₃Te₃O_{0.35}, respectively, upon cooling. The resistivity further increases upon cooling and reaches a maximum at 25 K, 11 K and 9 K, respectively, for three tellurides. Below these tem-

peratures, the resistivity recovers metallic-like transport of different character than that observed at higher temperatures.

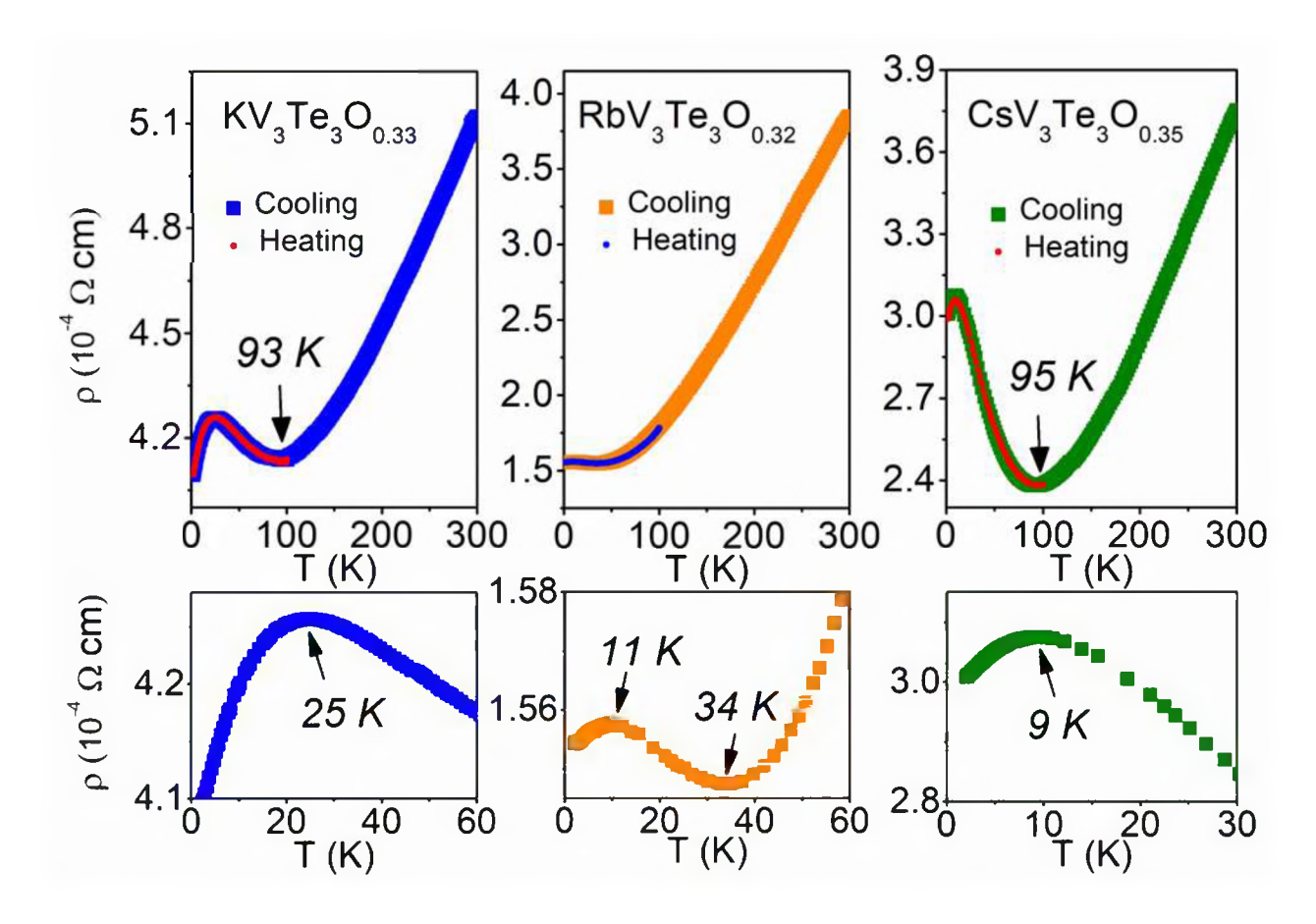


Figure 8. (a) Temperature dependent resistivity of KV₃Te₃O_{0.33}, RbV₃Te₃O_{0.32} and CsV₃Te₃O_{0.35} single crystals along the chain direction from 300 to 2 K. The lower panels highlight the low-temperature resistivity.

The electronic transitions of the three tellurides shown in Figure 8 were thermally reversible as evidenced by the absence of hysteresis upon cooling and heating curves below 100 K, suggesting if they are thermodynamic phase transitions then they are continuous in character. Considering the presence of the Q1D features in the compounds, the initial metal-semiconductor transition could be a Peierls distortion, as suggested in the isostructural AMo₃Q₃ system. Our band structure calculations of KV₃Te₃O_{0.33} (shown below in Theoretical electronic structures section) indicate that the V₃-triangle-trimerization, however, does not open a complete gap in the electronic structure. Additionally, no anomaly was observed in temperature-dependent heat capacity curve (Figure S15), eliminating a thermodynamic phase transition. Thus, a coherent Peierls transition is unlikely the origin of the insulating transport response.

For the three tellurides with oxygen atoms occupied, the oxygen disorder-induced electron localization in anisotropic Q1D system can increases and can contribute to the semiconductinglike up-turn in the resistivity. Based on single-crystal diffraction, the concentration of oxygen is $\delta \sim 0.33$ in the three tellurides AV₃Te₃O_{δ}. This partial occupation creates an intrinsic, random disorder potential in AV₃Te₃O_δ that is amplified by the local structural distortion found in the V₆O octahedron, leading to upturns in $\rho(T)$. The resistivity for a different CsV₃Te₃O_{0.35} crystal from the same batch was measured and the evolution of ρ is qualitatively similar, but the transition temperature changes (Figure S16), demonstrating that the role of the oxygen concentration plays in tuning the disorder potential which affect the semiconducting-like behavior arising from intrinsic defects. The resistivity data of CsV₃Te₃O_{0.35} from 100 to 50 K were fitted using both variable range hopping (VRH) and thermal activation (TA) models, respectively (Figure S17). The VRH model provides a better description of the semiconducting data, supporting the localizedelectron picture. Note that similar broad semiconducting-like transitions were also observed in isostructural Na_{1-x}Mo₃Se₃, which were suggested to result from substantial Na vacancy formation due to the high crystal growth temperature (1750 °C). [44] For our AV₃Te₃O_δ crystals, the synthesis temperature was relatively low (1000 °C) and single-crystal refinement indicated full occupation of the alkali metal site. Hence, the disorder in the AV₃Te₃O_δ crystals is mainly due to oxygen in the V₆ cluster octahedra. In addition, these metal-semiconductor-metal transitions can also be attributed to a Lifshitz-like transition, which will be discussed further below.

Last, magnetic susceptibilities of polycrystalline KV_3Se_3 and $KV_3Te_3O_{0.33}$ samples were measured from 2 to 300 K (Figure S18). Both compounds showed paramagnetic behavior without any magnetic phase transitions over the measured temperature range. The data fits well to the modified Curie-Weiss law, allowing us to determine effective V magnetic moments of 0.22 and $0.23\mu_B$ for KV_3Se_3 and $KV_3Te_3O_\delta$, respectively. The small moments suggest a low charge valence of V in the 133-type compounds due to the formation of V metallic bonds and delocalization of the spin density over multiple V sites. The θ values from our fits are close to zero (-7.03 K for KV_3Se_3 and -1.47 K for $KV_3Te_3O_\delta$), suggesting that the interaction between the magnetic moments in these compounds is very weak.

Theoretical electronic structures

To understand why some of the AV_3Q_3 structures incorporate oxygen while others do not, we firstly compared the electronic density of states (DOS) of the hypothetical "empty" compound KV₃Te₃ to that of KV₃Te₃O_{0,33} (Figure S19). The electronic DOS indicates both compounds are metallic with the Fermi level dominated by V 3d states. To understand whether these states exhibit bonding- and anti-bonding character, we performed a crystal orbital Hamiltonian population (COHP) analysis using the LOBSTER code. [45-48] The convention is to plot the negative COHP (-COHP, which is unitless) so that bonding interactions are positive whereas antibonding interactions are negative. For KV₃Te₃, the COHP of the V-V bonds within the a-b plane (Figure 9a) exhibit strong antibonding character at the Fermi level which leads to internal bond stresses and a chemically unstable compound. In KV₃Te₃O_{0.33}, the V-V bonds elongate, however, differently from KV₃Te₃, two different V₆ cluster octahedra are present: the oxygen-centered and the oxygen-free V-cluster. The COHP (Figure 9b) shows that the V-V bonds of the oxygen-free V-cluster are still strongly antibonding at the Fermi level, whereas the antibonding character of the V-V bonds of the oxygen-centered V-cluster is strongly reduced to give a nearly non-bonding interaction. These two changes together release the internal stress and stabilize the compound. Note that this result is quantitatively in agreement with the previous study by Wu et al. [40]

We next perform a similar COHP analysis for the V-V metallic bonds within the *a-b* plane of the selenide KV₃Se₃ in Figure 9c. In this case, the V-V bonds are inequivalent with one long and two short bonds. The symmetry of the two octahedral clusters is broken without oxygen incorporation. At the Fermi level, although the COHP for the long V-V bonds is strongly antibonding, the antibonding states of the short V-V bonds are strongly reduced stabilizing the shorts V-V bonds and then KV₃Se₃. Thus, the broken structural symmetry in the selenide serves a similar role as oxygen incorporation in the telluride. Summarizing, the intrinsic internal stress of these V-cluster-based Q1D materials is released with the introduction of interstitial oxygen atoms at the centers of the V₆ cluster octahedra in KV₃Te₃ and through a structural distortion, which make the V-V bonds inequivalent, in KV₃Se₃.

Our COHP analysis clearly indicates the instability of V_6 cluster octahedra in $AV_3Q_3O_6$, which can be solved either by incorporating the oxygen at centered site, or by distorting the oc-

tahedra to reduce the symmetry. The scenario in $KV_3Te_3O_{0.33}$ is the former manner whereas the KV_3Se_3 adopts the later one. This discrepancy can be explained by considering the lattice mismatch of double-walled $(V_3Q_3)^-$ nanowire motif: for KV_3Se_3 , the oxygen-involved V-cluster could be too large to insert into the selenium nanotube.

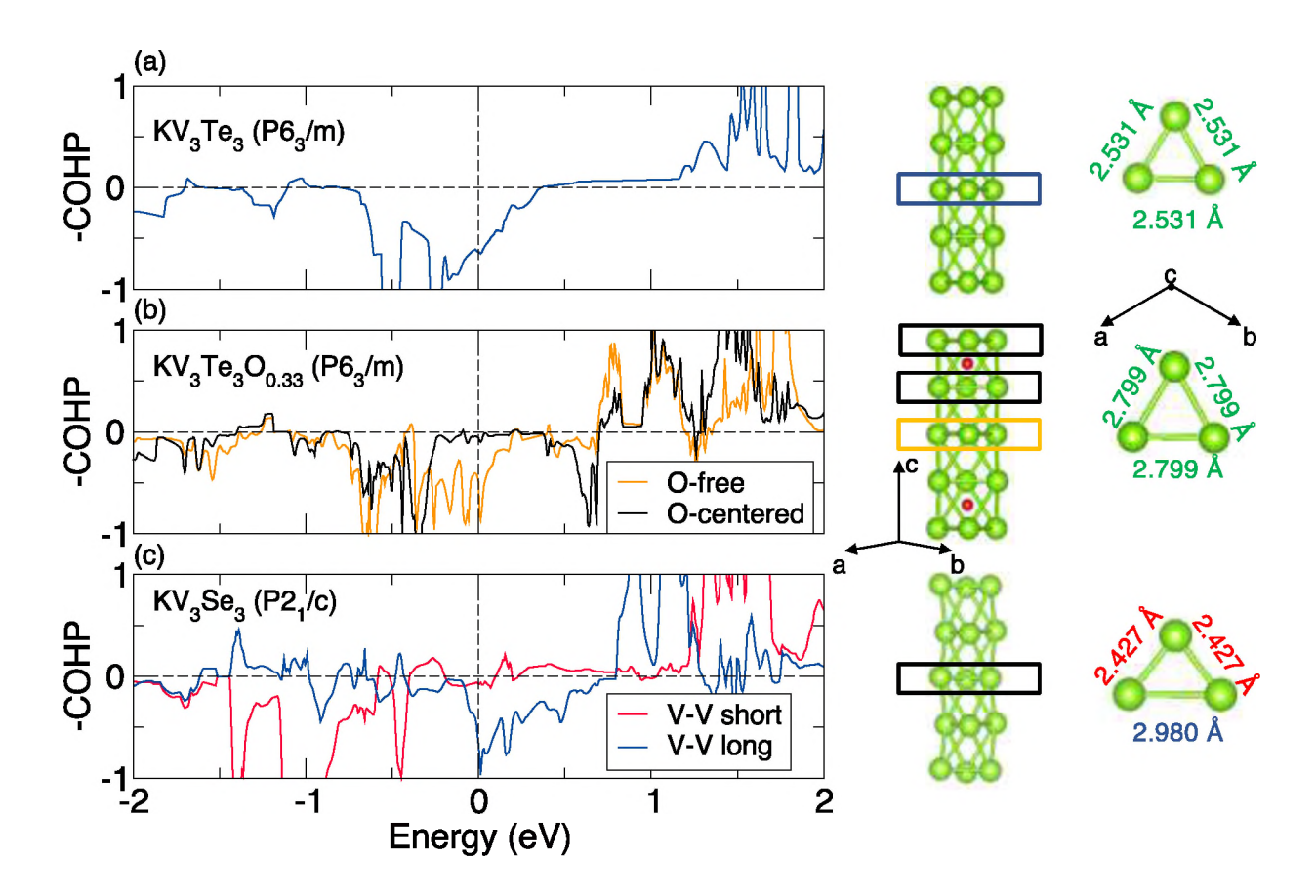


Figure 9. Crystal orbital Hamiltonian population (COHP) analysis of the V-V bonds parallel to the *a-b* plane for (a) KV₃Te₃, (b) KV₃Te₃O_{0.33}, and (c) KV₃Se₃. Bonding interactions are positive whereas antibonding interactions are negative. The three different configurations of V-cluster are shown on right side (green sphere: V and red sphere: O)

Consistent with our resistivity measurements, our calculated densities-of-states (DOS) of KV₃Se₃, including spin-orbit interactions, show that the Q1D compound remains metallic regard-

less of the distorted-structure model considered (Figure 10a and Figure S20). Compared with the $P6_3/m$ structure, the $P2_1/m$ distortion decreases the DOS at the Fermi level (Figure 10b), which are mainly contributed by the V 3d orbitals. The electronic properties of the $P2_1$ and $P2_1/c$ phases are similar to those of the $P2_1/m$ phase (Figure 10a), however, the number of states at the Fermi level is further reduced in the $P2_1/c$ phase (Figure 10b). All low energy monoclinic phases exhibit similar band dispersions (Figure S20) with almost flat bands near the Fermi level along the Z-C-D-E direction in the $k_z = 1/2$ plane.

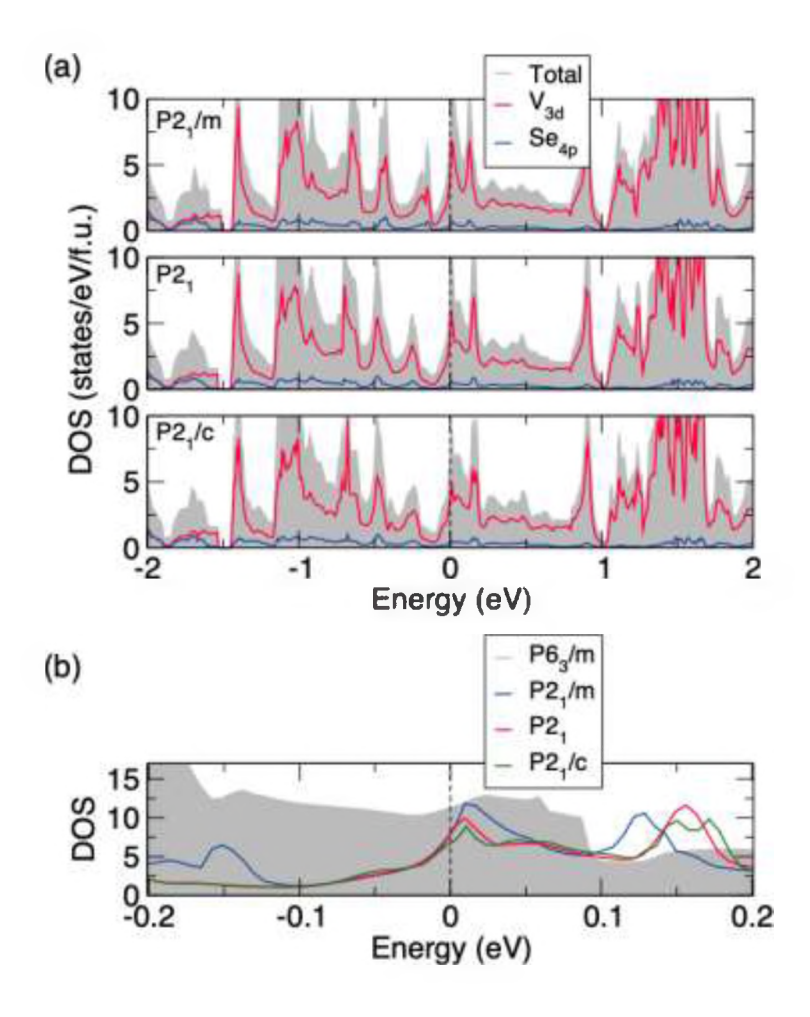


Figure 10. (a) Total and partial density-of-states (DOS) of monoclinic KV₃Se₃ in $P2_1/m$, $P2_1$ and $P2_1/c$ phases. (b) Enlarged total DOS of three monoclinic phases near Fermi level compared with the average structure of $P6_3/m$ symmetry.

The trimerized $P6_3/m$ phase exhibits quasi-one-dimensional metallic behavior with a larger number of states at the Fermi level than the trimer-free $P6_3/m$ model, owing to a reorganization of states on the Fermi surface. Figure 11 shows that the Fermi surface is nearly gapped along the A-L-H-A trajectory comprising k_2 =1/2, suggesting that the experimental semiconducting behavior may be due to a Lifshitz-like transition leading to reduced number of carriers and increased band effective masses as the Fermi surface reconstructs from the vibronic instability. A small electron pocket remains along Γ -A; therefore, changes in oxygen content δ could also shift the chemical potential and the available number of carriers for transport. The second semiconductor-metal transition with temperature further decreased could also result from a change of the Fermi surface topology as well. Similar thermally-driven broad metal-semiconductor-metal transitions were observed in other tellurides, including Q1D InTe_{1- δ} and Q2D ZrTe₅, which were attributed to a Lifshitz transition with a change of the Fermi surface topology. [49][50]

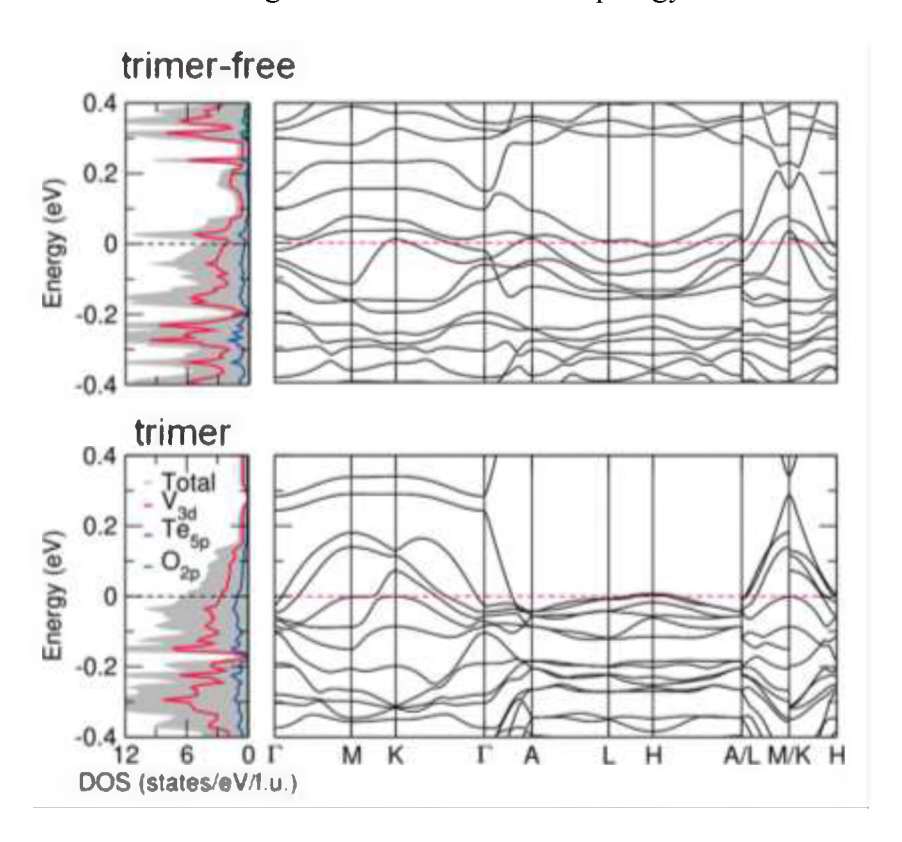


Figure 11. Total, partial DOS, and band structure of KV₃Te₃O_{0.33} near the Fermi level (0 eV) for the trimer-free and trimer models. The V₃-triangle-trimerization removes the van Hove singularity located just above the Fermi level in the trimer-free structure.

Conclusions

We observed the surprising presence of oxygen on the reduced cluster column chalcogenide compounds of vanadium $AV_3Q_3O_\delta(A = K, Rb, Cs \text{ and } Q = Se, Te)$. The salt flux of A_2Q_x was found to be efficient in growing these low-dimensional vanadium cluster compounds, which adopt the TlFe₃Te₃-type structure ($P6_3/m$ symmetry) and contain infinite (V_3Q_3) double-walled columnar chains. X-ray diffraction revealed distinct oxygen presence in these compounds: the (V_3Q_3) double-walled columnar chains in the tellurides $AV_3Te_3O_\delta$ are trimerized to form V_9 clusters with oxygen-centered found between the trimers. The KV₃Se₃ compound however is oxygen-free. Using pair distribution function analysis of synchrotron X-ray total scattering data, we observed a local distortion in the ab plane on these "empty" V₆ cluster octahedra in KV₃Se₃ while KV₃Te₃O_{0.33}, with the centered oxygen, shows an out-of-plane V₃-triangle-trimerization. These distinct distortions indicate how centered atoms within the octahedra alter the local structural stability. The strong instability and distortions of the cluster columns in $AV_3Q_3O_\delta$ are unusual and may provide a fertile ground to induce novel physics and chemistry by carrying out chemical doping or physical pressure studies. In addition, we showed AV₃Te₃O_δ exhibits a metal-semiconductor-metal transition, indicating an interplay between these local structure changes, oxygen centered V₆ disorder, and Fermi surface topology. Because the TlFe₃Te₃-type phase with the $P6_3/m$ space group can host nontrivial fermions, [25] the AV₃Q₃O₈ may prove to be promising in the search for topological semimetals whereby the electronic state is tuned by changes in oxygen concentration.

Experiment section

Synthesis. The polycrystalline sample of KV₃Se₃ and KV₃Te₃O_{δ} was synthesized by conventional solid-state reaction. Powders of V (99.5%, Alfa Aesar), Se (99.999%, Aladdin), Te (99.99%, Aladdin) were mixed and ground in an agate mortar in a glove-box, followed by cold-pressing into disks (1 mm in diameter) with a 200 kg/cm² uniaxial stress. The disks were put into alumina crucibles together with the addition of K (99.8%, Alfa Aesar) using target molar ration (A: V: Q = 1: 3: 3) and sealed into quartz tube under vacuum (10⁻³ mbar). The tube was firstly heated to 200 °C to react the alkali metal for 10 hours. Then they were heated to 950 °C, held for 24 hours and then cooled down to 400 °C with 50 °C per hour and kept for 24 hours at 400 °C. Finally the tubes were cooled down to room temperature by switching off the furnace.

Crystal Growth. Single crystals in this work were grown using A₂Q_x flux. For KV₃Se₃, K₂Se (1.4043 g), V (0.3901 g) and Se (0.7055 g) with a total amount of 2.5 g were mixed in the target molar ration (A:V:Te = 7:3:7) in glove-box and loaded into alumina crucible. An alumina filter was also placed on the top of the crucible. The crucible and filter were loaded into fused silica tubes and sealed under vacuum at $\sim 5 \times 10^{-3}$ mbar, heated to 1000 °C in 12 h, held there for 24 hours and cooled to 650 °C in 24-48 hours. After being held at 650 °C for a few hours, the tube was removed from the furnace and immediately centrifuged to remove excess K2Sex flux. Residual flux on the surface of the crystals was removed by soaking in the product in ethanol for 2-3 hours, followed by rinsing with acetone. For growing AV₃Te₃O_δ, the starting molar ration was changed to A:V:Te = 7:3:12 by mixing the K_2 Te (1.8396 g), V (0.3903 g), Te (2.7701 g) for $KV_3Te_3O_{0.33}$; Rb_2Te (2.2891 g), V (0.3348 g), Te (2.3761 g) for $RbV_3Te_3O_{0.32}$; and Cs_2Te (2.6334 g), V (0.2923 g), Te (2.0743 g) for CsV₃Te₃O_{0.35}, with the total amount of 5 g. The following synthetic process was the same with that of KV₃Se₃. All the crystals formed as the needle-like crystals with 3-4 mm length. The rubidium and cesium metal were obtained from Strem Chemicals, Inc. (99.9%). The K₂Se, K₂Te, Rb₂Te and Cs₂Te were synthesized by reacting stoichiometric amounts of the elements in liquid ammonia as described in literature. [51] The yield of AV₃Te₃O_{δ} from this crystal growth experiment is ~75 % by weight with a small amount of binary phase containing V and Te. The yield of KV₃Se₃ is around 50 %, and our attempts to improve the yield by changing the starting composition were unsuccessful.

Structure and Composition Determination. The composition analysis of these four compounds was done by X-ray analysis with an energy dispersive spectroscopy (EDS) in a field-emission scanning electron microscope. Crystals with appropriate size were selected for single-crystal X-ray diffraction (SCXRD) using Bruker D8 Venture diffractometer at 50kV and 1.4 mA with Mo K α radiation ($\lambda = 0.71073$ Å). Integration was done using Bruker SAINT software package and absorption correction were done using the MultiScan method. Crystal structures were solved by direct methods and refined by full-matrix least-squares on F² using the OLEX2 program package. All data were collected at room temperature under nitrogen flow. Powder X-ray diffraction (PXRD) was collected at room temperature on a PANalytical diffractometer (X'Pert PRO MRD) equipped with CuK α radiation (λ =1.5148 Å). The synchrotron powder X-ray diffraction (SPXRD) was collected at the beam line 11-BM of the advanced photon source (APS), Argonne National Laboratory with X-ray radiation (λ =0.45785Å). Fine powder sample

Physical Property Measurements. Magnetization susceptibility of polycrystalline samples was measured using Quantum Design magnetic property measurement system (MPMS-5T) with the field H = 1000 Oe. Resistivity and specific heat capacity were measured on the single crystal samples by using a physical property measurement system (PPMS-9T). The electrical resistivity was measured in a standard four-probe method using platinum wires (diameter of 0.0508 mm, 99.95%, Alfa Aesar) attached onto the needle-like crystals by Ag paste (TED PELLA). Several pieces of the crystals were pressed into a bullet and used for the specific heat measurements. All sample preparation was done in a glovebox filled with argon gas to prevent the oxidation of sample surface.

Density Functional Theory Calculations. We performed first-principles DFT calculations within the Perdew-Burke-Ernzerhof exchange-correlation functional revised for solids (PBEsol)^[56] as implemented in the Vienna Ab initio Simulation Package (VASP)^[57] with the projector augmented wave (PAW) approach^[58] to treat the core and valence electrons using the following electronic configurations: $3s^2 3p^6 4s^1$ (K), $3s^2 3p^6 4s^2 3d^3$ (V), $4s^2 4p^4$ (Se), $5s^2 5p^4$ (Te), $2s^2 2p^4$ (O) with a 600 eV planewave cutoff. The Brillouin zone was sampled with a 8 × 8 × 8 Γ-centered *k*-point mesh and integrations performed using Gaussian smearing (20 meV width). The electronic properties were calculated with the inclusion of spin-orbit interactions. For all calculations, we relaxed the atomic positions such that the forces < 0.1 meV A⁻¹. The experimental lattice parameters are used in all the calculations. Phonons were calculated using the frozen-phonon ap-

proach with finite displacements of 0.01 Å and a $2 \times 2 \times 2$ and $1 \times 1 \times 1$ supercell for KV₃Se₃ and KV₃Te₃O_{0.33}, respectively. Moreover, a 600 eV planewave cutoff, a phonon energy tolerance of 10^{-8} eV, and a $8 \times 8 \times 8$ Γ-centered k-point mesh were used. Phonon frequencies were calculated from the force constants using the PHONOPY code. Convergence of the phonon frequencies with respect planewave cutoff and k-point mesh was considered achieved for change in frequency less than 7 cm⁻¹. The dynamic instability of the $P2_1/m$ phase of KV₃Se₃ is confirmed by the energy gain obtained by linear interpolation between the $P2_1/m$ and the $P2_1/c$ and $P2_1$ structures derived from the phonon instabilities (Fig. S9b).

Associated content

Supporting information. The supporting Information is available free at

Stability, elemental mapping, PDF analysis, heat capacity, resistivity, magnetic susceptibility and density of states (PDF)

Crystallographic information (CIF)

Author information

Corresponding Authors

*wxyuanwz@163.com

*m-kanatzidis@northwestern.edu

Author Contributions

 $^{\nabla}$ Zhongnan Guo and Fan Sun contributed equally to this work.

Notes

The authors declare no competing financial interest.

Acknowledgements

Work at Northwestern University (synthesis, physical properties measurements and DFT calculations) was supported by the National Science Foundation's (NSF) MRSEC program (DMR-1720139) at the Materials Research Center of Northwestern University. J.M.R. was also supported by NSF under DMR-2011208. W.Y and Z.G. acknowledge the support from the National Natural Science Foundation of China (Grant Nos. 51532010, 51872028 and 51832010). Work at Argonne National Laboratory (magnetic property measurements) was support by the U.S. De-

partment of Energy, Office of Science, Basic Energy Sciences, Materials Science and Engineering Division. Use of the Advanced Photon Source (APS) was supported by the U. S. Department of Energy, Office of Science, Office of Basic Energy Sciences, under Contract No. DE-AC02-06CH11357. We thank Dr. Leighanne Gallington at APS for assisting in the PDF measurements. We also thank Dr. Haijie Chen at Northwestern University and Dr. Xiaolong Chen at the Institute of physics, Chinese Academy of Sciences for helpful discussions.

References

- [1] Chen, C.-T.; Suslick, K. S. One-dimensional coordination polymers: Applications to material science. *Coordin. Chem. Rev.* **1993**, 128, 293-322.
- [2] Luttinger, J. M. An exactly soluble model of a many fermion system. *J. Math. Phys.* **1963**, 4, 1154-1162.
- [3] Haldane, F. D. M. Nonlinear field theory of large-spin Heisenberg antiferromagnets: semi-classically quantized solitons of the one-dimensional easy-axis Néel state. *Phys. Rev. Lett.* **1983**, 50, 1153-1156.
- [4] Armici, J. C.; Decroux, M.; Fischer, Ø. A new pseudo-one-dimensional superconductor: Tl₂Mo₆Se₆. *Solid State Commun.* **1980**, 33, 607-611.
- [5] Amberger, E.; Polborn, K.; Grimm, P. Superconductivity in the Nb cluster compounds Nb₃(X,Y)₄ with X, Y = S, Se, Te. *Solid State Commun.* **1978**, 26, 943-947.
- [6] Johnston, D. C.; Maki, M.; Grüner, G. Influence of charge density wave fluctuations on the magnetic susceptibility of the quasi-one-dimensional conductor (TaSe₄)₂I. Solid State Commun. 1985, 53, 5-8.
- [7] Selte, K.; Kjekshus, A. The crystal structures of Nb₃Se₄ and Nb₃Te₄. *Acta Cryst.* **1964**, 17, 1568-1572.
- [8] Lei, H.; Ryu, H.; Frenkel, A. I.; Petrovic, C. Anisotropy in BaFe₂Se₃ single crystals with double chains of FeSe tetrahedra. *Phys. Rev. B* **2011**, 84, 214511.
- [9] Yamauchi, T.; Hirata, Y.; Ueda, Y.; Ohgushi, K. Pressure-Induced Mott Transition Followed by a 24-K Superconducting Phase in BaFe₂Se₃. *Phys. Rev. Lett.* **2015**, 115, 246402.
- [10] Takahashi, H.; Sugimoto, A.; Nambu, Y.; Yamauchi, T.; Hirata, Y.; Kawakami, T.; Avdeev, M.; Matsubayashi, K.; Du, F.; Kawashima, C.; Soeda, H.; Nakano, S.; Uwatoko, Y.;

- Ueda, Y.; Sata, T. J.; Ohgushi, K. Pressure-induced superconductivity in the iron-based ladder material BaFe₂S₃. *Nat. Mater.* **2015**, 14, 1008-1012.
- [11] Hönle, W.; Schnering, H. G. von; Lioka, A.; Yvon, K. New compounds with infinite chains of face-condensed octahedral Mo6 clusters: InMo₃Se₃, InMo₃Te₃, TlMo₃Se₃ and TlMo₃Te₃. *J. Less-Common Met.* **1980**, 71, 135-145.
- [12] Potel, M.; Chevrel, R.; Sergent, M.; Armici, J. C.; Decroux, M.; Fischer, Ø. New pseudo-one-dimensional metals: M₂Mo₆Se₆ (M= Na, In, K, TI), M₂Mo₆Se₆ (M= K, Rb, Cs), M₂Mo₆Te₆ (M= In, TI). Solid State Commun. **1980**, 35, 286-290.
- [13] Tarascon, J. M.; DiSalvo, F. J.; Waszczak, J. V. Physical properties of several M₂Mo₆X₆ compounds (M= group IA metal; X= Se, Te). *Solid State Commun.* **1984**, 52, 227-231.
- [14] Hor, P. H.; Fan, W. C.; Chou, L. S.; Meng, R. L.; Chu, C. W.; Tarascon, J. M.; Wu, M. K. Study of the metal-semiconductor transition in Rb₂Mo₆Se₆, Rb₂Mo₆Te₆ and Cs₂Mo₆Te₆ under pressures. *Solid State Commun.* **1985**, 55, 231-235.
- [15] Badding, M. E.; Gitzendanner, R. L.; Ziebarth, R. P.; DiSalvo, F. Electrical and magnetic properties of tantalum silicon telluride and isostructural compounds. *J. Mater. Res. Bull.* **1994**, 29, 327-336.
- [16] Heinrich, C. P.; Panthöfer, M.; Tremel, W. Ta₄FeTe₄: a new material for metallic single molecular wires. *Eur. Phys. J. B.* **2012**, 85, 221.
- [17] Bao, J.-K.; Tang Z.-T.; Jung, H. J.; Liu, J.-Y.; Liu, Y.; Li, L., Li, Y.-K.; Xu, Z.-A.; Feng, C.-M.; Chen, H.; Chung D. Y.; Dravid, V. P.; Kanatzidis, M. G. Unique [Mn₆Bi₅]— Nanowires in KMn₆Bi₅: A Quasi-One-Dimensional Antiferromagnetic Metal. *J. Am. Chem. Soc.* **2018**, 140, 4391-4400.
- [18] Jung, H. J.; Bao, J.K., Chung, D. Y.; Kanatzidis, M. G.; Dravid, V. P. Unconventional Defects in a Quasi-One-Dimensional KMn₆Bi₅. *Nano Lett.* **2019**, 19, 7476-7486.
- [19] Gibson, Q. D.; Schoop, L.M.; Muechiler, L.; Xie, L. S.; Hirschberger, M.; Ong, N. P.; Car, R.; Cava, R. Three-dimensional Dirac semimetals: Design principles and predictions of new materials. J. *Phys. Rev. B* 2015, 91, 205128.
- [20] Schoop, L. M.; Ali, M. N.; Straβer, C.; Topp, A.; Varykhalov, A.; Marchenko, D.; Duppel, V.; Parkin, S. S. P.; Lotsch, B. V.; Ast, C. R. Dirac cone protected by non-symmorphic symmetry and three-dimensional Dirac line node in ZrSiS. *Nat. Commun.* **2016**, *7*, 11696.

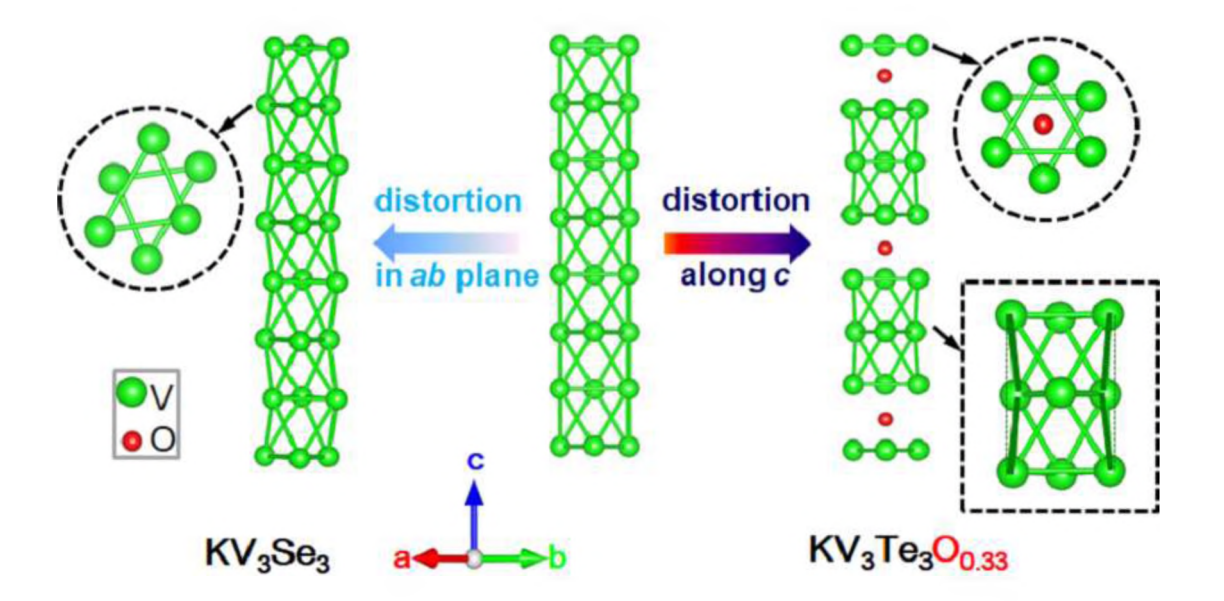
- [21] Singha, R.; Pariari, A. K.; Satpati, B.; Mandal, P. Large nonsaturating magnetoresistance and signature of nondegenerate Dirac nodes in ZrSiS. *Natl. Acad. Sci. U. S. A.* **2017**, 114, 2468-2473.
- [22] Khoury, J. F.; Rettie, A. J. E.; Khan, M. A.; Ghimire, N. J.; Robredo, I.; Pfluger, J. E.; Pal, K.; Wolverton, C.; Bergara, A.; Jiang, J. S.; Schoop, L. M.; Vergniory, M. G.; Mitchell, J. F.; Chung, D. Y.; Kanatzidis, M. G. A New Three-Dimensional Subsulfide Ir₂In₈S with Dirac Semimetal Behavior. *J. Am. Chem. Soc.* 2019, 141, 48, 19130-19137.
- [23] Khoury, J. F.; Rettie, A. J. E.; Robredo, I.; Krogstad, M. J.; Malliakas, C. D.; Bergara, A.; Vergniory, M. G.; Osborn, R.; Rosenkranz, S.; Chung, D. Y.; Kanatzidis, M. G. The Subchalcogenides Ir₂In₈Q (Q = S, Se, Te): Dirac Semimetal Candidates with Re-entrant Structural Modulation. *J. Am. Chem. Soc.* **2020**, 142, 13, 6312-6323.
- [24] Nakayama, K.; Wang, Z.; Trang, C. X.; Souma, S.; Rienks, E. D. L.; Takahashi, T.; Ando, Y.; Sato, T. Observation of Dirac-like energy band and unusual spectral line shape in quasi-one-dimensional superconductor Tl₂Mo₆Se₆. *Phys. Rev. B* 2018, 98, 140502.
- [25] Liu, Q.; Zunger, A. Predicted realization of cubic Dirac fermion in quasi-one-dimensional transition-metal monochalcogenides. *Phys. Rev. X* **2017**, 7, 021019.
- [26] Huang, S.-M.; Hsu, C.-H.; Xu, S.-Y.; Lee, C.-C.; Shiau, S.-Y.; Lin, H.; Bansil, A. Topological superconductor in quasi-one-dimensional Tl_{2-x}Mo₆Se₆. *Phys. Rev. B* 2018, 97, 014510.
- [27] Klepp, K.; Boller, H. Die Kristallstruktur von TlFe₃Te₃. *Monatsh. Chem.* **1979**, 110, 677-684.
- [28] Sun, F.; Guo, Z.; Liu, N.; Wu, D.; Lin, J.; Cheng, E.; Ying, T.; Li, S.; Yuan, W. Cs_{0.9}Ni_{3.1}Se₃: A Ni-Based Quasi-One-Dimensional Conductor with Spin-Glass Behavior. *Inorg. Chem.* **2018**, 57, 3798-3804.
- [29] Lin, J.; Deng, J.; Guo, Z.; Cheng, E.; Sun, F.; Liu, N.; Wang, B.; Li, S.; Yuan, W. Structure and physical properties of Ni-based quasi-one-dimensional selenides Rb_{0.9}Ni_{3.1}Se₃ and K_{0.7}Ni_{3.1}Se₃. *J. Alloy Compd.* **2019**, 793, 425-432.
- [30] Bao, J.-K.; Liu, J.-Y.; Ma, C.-W.; Meng, Z.-H.; Tang, Z.-T.; Sun, Y.-L.; Zhai, H.-F.; Jiang, H.; Bai, H.; Feng, C.-M.; Xu, Z.-A.; Cao, G.-H. Superconductivity in Quasi-One-Dimensional K₂Cr₃As₃ with Significant Electron Correlations. *Phys. Rev. X* **2015**, 5, 011013.

- [31] Tang, Z.-T.; Bao, J.-K.; Liu, Y.; Sun, Y.-L.; Ablimit, A.; Zhai, H.-F.; Jiang, H.; Feng, C.-M.; Xu, Z.-A.; Cao, G.-H. Unconventional superconductivity in quasi-one-dimensional Rb₂Cr₃As₃. *Phys. Rev. B* **2015**, 91, 020506.
- [32] Tang, Z.-T.; Bao, J.-K.; Wang, Z.; Bai, H.; Jiang, H.; Liu, Y.; Zhai, H.-F.; Feng, C.-M.; Xu, Z.-A.; Cao, G.-H. Superconductivity in quasi-one-dimensional Cs₂Cr₃As₃ with large interchain distance. *Sci. China Mater.* **2015**, 58, 16-20.
- [33] Taddei, K. M.; Xing, G.; Sun, J.; Fu, Y.; Li, Y.; Zheng, Q.; Sefat, A. S.; Singh, D. J.; Cruz, C. de la. Frustrated Structural Instability in Superconducting Quasi-One-Dimensional K₂Cr₃As₃. *Phys. Rev. Let.*, **2018**, 121, 187002.
- [34] Bao, J.-K.; Li, L.; Tang, Z.-T.; Liu, Y.; Li, Y.-K.; Bai, H.; Feng, C.-M.; Xu, Z.-A.; Cao, G.-H. Cluster spin-glass ground state in quasi-one-dimensional K₂Cr₃As₃. *Phys. Rev. B* **2015**, 91, 180404.
- [35] Tang, Z.-T.; Bao, J.-K.; Liu, Y.; Bai, H.; Jiang, H.; Zhai, H.-F.; Feng, C.-M.; Xu, Z.-A.; Cao, G.-H. Synthesis, crystal structure and physical properties of quasi-one-dimensional ACr₃As₃ (A = Rb, Cs). *Sci. China Mater.* **2015**, 58, 543-549.
- [36] Xing, G.; Shang, L.; Fu, Y.; Ren, W.; Fan, X.; Zheng, W.; Singh, D. J. Structural instability and magnetism of superconducting KCr₃As₃. *Phys. Rev. B* **2019**, 99, 174508.
- [37] Taddei, K. M.; Sanjeewa, L. D.; Lei, B.-H.; Fu. Y.; Zheng, Q.; Singh, D. J.; Sefat, A. S.; Cruz, C. de la. Tuning from frustrated magnetism to superconductivity in quasi-one-dimensional KCr₃As₃ through hydrogen doping. *Phys. Rev. B* **2019**, 100, 220503.
- [38] Xiang, J.J.; Yu, Y.-L.; Wu, S.-Q.; Li, B.-Z.; Shao, Y.-T.; Tang, Z.-T.; Bao, J.-K.; Cao, G.-H. Superconductivity induced by aging and annealing in K₁₋₈Cr₃As₃H_x. *Phys. Rev. Mater.* **2019**, 3, 114802.
- [39] Wu, S.-Q., Chao, C.; Cao, G.-H.; Lifshitz transition and nontrivial H-doping effect in the Cr-based superconductor K_{1-δ}Cr₃As₃H_x. *Phys. Rev. B* **2019**, 100, 155108.
- [40] Wu, E. J.; Pell, M. A.; Genin, H. S.; Ibers, J. A. Synthesis, characterization, and electronic structure of KV₃Te₃O_{0.42}. *J. Alloy Compd.* **1998**, 278, 123-129.
- [41] Valldor, M.; Merz, P.; Prots, Y.; Schelle, W. Bad-Metal-Layered Sulfide Oxide CsV₂S₂O. *Eur*, *J*, *Inorg. Chem.* **2016**, 23-27.
- [42] Ablimit, A.; Sun, Y.-L.; Jiang, H.; Wu, S.-Q.; Liu, Y.-B.; Cao, G.-H. Weak metal-metal transition in the vanadium oxytelluride Rb₁₋₈V₂Te₂O. *Phys. Rev. B* **2018**, 97, 214517.

- [43] Baber, W. G., The contribution to the electrical resistance of metals from collisions between electrons. *P. Roy. Soc. Lond. A Mat.* **1937**, 158, 383.
- [44] Petrovic, A. P.; Ansermet, D.; Chernyshov, D.; Hoesch, M.; Salloum, D.; Gougeon, P.; Potel, M.; Boeri, L.; Panagopoulos, C. A disorder-enhanced quasi-one-dimensional superconductor. *Nature Comm.* 2016, 7, 12262.
- [45] Deringer, V. L.; Tchougréeff, A. L.; Dronskowski, R., Crystal orbital hamilton population (COHP) analysis as projected from plane-wave basis sets. *J. Phys. Chem. A* **2011**, 115, 5461-5466.
- [46] Maintz, S.; Deringer, V. L.; Tchougréeff, A. L.; Dronskowski, R. LOBSTER: A tool to extract chemical bonding from plane-wave based DFT. *J. Comput. Chem.* **2016**, 37, 1030-1035.
- [47] Maintz, S.; Esser, M.; Dronskowski, R. Efficient rotation of local basis functions using real spherical harmonics, *Acta Phys. Pol. B* **2016**, 47, 1165-1175.
- [48] Maintz, S.; Deringer, V. L.; Tchougréeff, A. L.; Dronskowski, R. Analytic projection from plane-wave and PAW wavefunctions and application to chemical-bonding analysis in solids. *J. Comput. Chem.* **2013**, 34, 2557-2567.
- [49] Back, S. Y.; Kim, Y.-K.; Cho, H.; Han, M.-K.; Kim, S.-J.; Rhyee, J. S., Temperature-Induced Lifshitz Transition and Charge Density Wave in InTe_{1-δ} Thermoelectric Materials. *ACS Appl. Energ. Mater.* **2020**, 3, 3628-3636.
- [50] Zhang, Y.; Wang, C.; Yu, L.; Liu, G.; Liang, A.; Huang, J.; Nie, S.; Sun, X.; Zhang, Y.; Shen, B.; Liu, J.; Weng, H.; Zhao, L.; Chen, G.; Jia, X.; Hu, C.; Ding, Y.; Zhao, W.; Gao, Q.; Li, C.; He, S.; Zhao, L.; Zhang, F.; Zhang, S.; Yang, F.; Wang, Z.; Peng, Q.; Dai, X.; Fang, Z.; Xu, Z.; Chen, C.; Zhou, X.J. Electronic evidence of temperature-induced Lifshitz transition and topological nature in ZrTe₅. *Nature Comm.* **2017**, 8, 15512.
- [51] Hanko, J. A.; Sayettat. J.; Jobic, S.; Brec, R.; Kanatzidis, M. G. A₂CuP₃S₉ (A = K, Rb), Cs₂Cu₂P₂S₆, and K₃CuP₂S₇: New Phases from the Dissolution of Copper in Molten Polythiophosphate Fluxes. *Chem. Mater.* **1998**, 10, 3040-3049.
- [52] Dolomanov, O. V.; Bourhis, L. J.; Gildea, R. J.; Howard, J. A.; Puschmann, H. OLEX2: a complete structure solution, refinement and analysis program. J. Appl. Cryst. 2009, 42, 339-341.
- [53] Rodriguez-Carajal, Recent advances in magnetic structure determination by neutron powder diffraction. *Phys. B* **1993**, 192, 55-69.

- [54] Qiu, X.; Thompson, J. W.; Billinge, S. J. L. PDFgetX2: a GUI-driven program to obtain the pair distribution function from X-ray powder diffraction data. *J. Appl. Cryst.* **2004**, 37, 678
- [55] Farrow, C. L.; Juhas, P.; Liu, J. W.; Bryndin, D.; Božin, E. S.; Bloch, J.; Proffen, Th; Billinge, S. J. L. PDFfit2 and PDFgui: computer programs for studying nanostructure in crystals. *J. Phys-Condens. Mat.* **2007**, 19, 335219.
- [56] Perdew, J. P.; Ruzsinszky, A.; Csonka, G. I.; Vydrov, O.A.; Scuseria, G. E.; Constantin, L. A.; Zhou, X.; Burke, K. Restoring the density-gradient expansion for exchange in solids and surfaces. *Phys. Rev. Let.*, 2008, 100, 136406.
- [57] Kresse, G.; Furthmüller, J. Efficiency of ab-initio total energy calculations for metals and semiconductors using a plane-wave basis set. *Comp. Mater. Sci.* **1996**, 5, 15.
- [58] Blöchl, P. E.; Jepsen, O.; Andersen, O. K. Improved tetrahedron method for Brillouin-zone integrations. *Phys. Rev. B* **1994**, 49, 16223.
- [59] Togo, A.; Oba, F.; Tanaka, I. First-principles calculations of the ferroelastic transition between rutile-type and CaCl₂-type SiO₂ at high pressures. *Phys. Rev. B* **2008**, 78, 134106.
- [60] Togo, A. Phonopy, https://phonopy.github.io/phonopy/ (accessed 2021-03-09).

TOC Graphic



Supporting Information for:

Local distortions and metal-semiconductor-metal transition in quasi-one-dimensional nanowire compounds $AV_3Q_3O_\delta$ (A=K, Rb, Cs and Q=Se, Te)

Zhongnan Guo,^{a,b,∇} Fan Sun,^{a, ∇} Danilo Puggioni,^c Yubo Luo,^b Xiaotong Li,^b Xiuquan Zhou,^d Duck Young Chung,^d Erjian Cheng,^e Shiyan Li,^e James M. Rondinelli,^c Wenxia Yuan,^{*a} and Mercouri G. Kanatzidis^{*b,d}

^a Department of Chemistry, School of Chemistry and Biological Engineering, University of Science and Technology Beijing, Beijing 100083, China

^b Department of Chemistry, Northwestern University, Evanston, Illinois 60208, United States

^c Department of Materials Science and Engineering, Northwestern University, Evanston, Illinois 60208, United States

^d Materials Science Division, Argonne National Laboratory, Lemont, Illinois 60439, United
States

^e State Key Laboratory of Surface Physics, Department of Physics and Laboratory of Advanced
Materials, Fudan University, Shanghai 200433, China

Stability, elemental mapping and structure

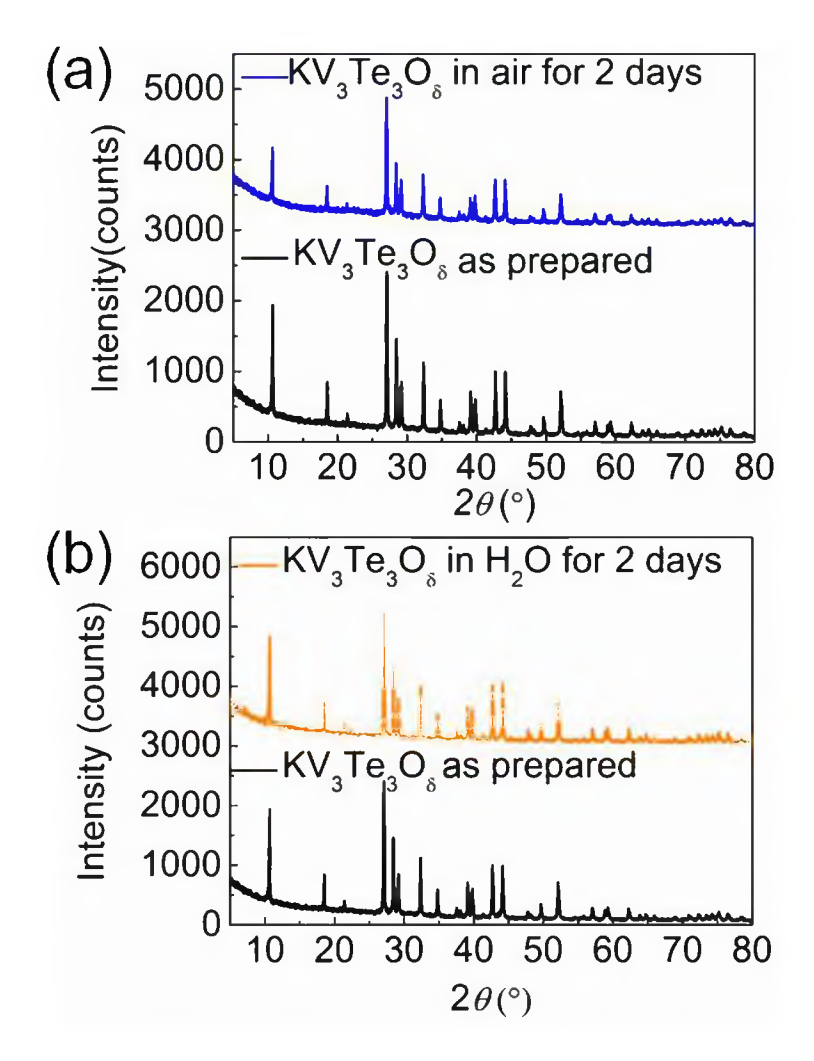


Figure S1. Powder X-ray diffraction patterns of $KV_3Te_3O_\delta$ polycrystalline samples undergoing the (a) ambient and (b) aqueous condition after 2 days compared with the pristine one.

To investigate the stability of these Q1D V-based chalcogenides, we kept $KV_3Te_3O_\delta$ polycrystalline samples in air and water for 2 days. The PXRD patterns in Figure S1 dot not change after these treatments, indicating the good stability of $KV_3Te_3O_\delta$ in air and aqueous condition. KV_3Se_3 shows the same stability with $KV_3Te_3O_\delta$ in air and water based on the PXRD patterns (not shown here).

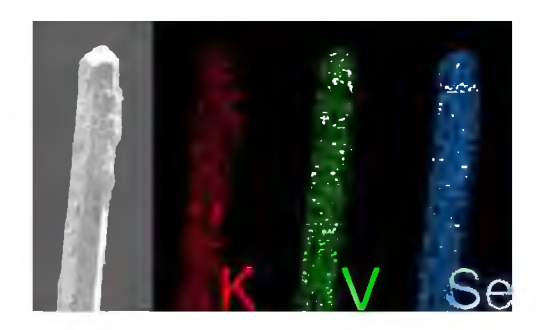


Figure S2. Elemental mapping of a KV₃Se₃ crystal, showing its homogeneous nature.

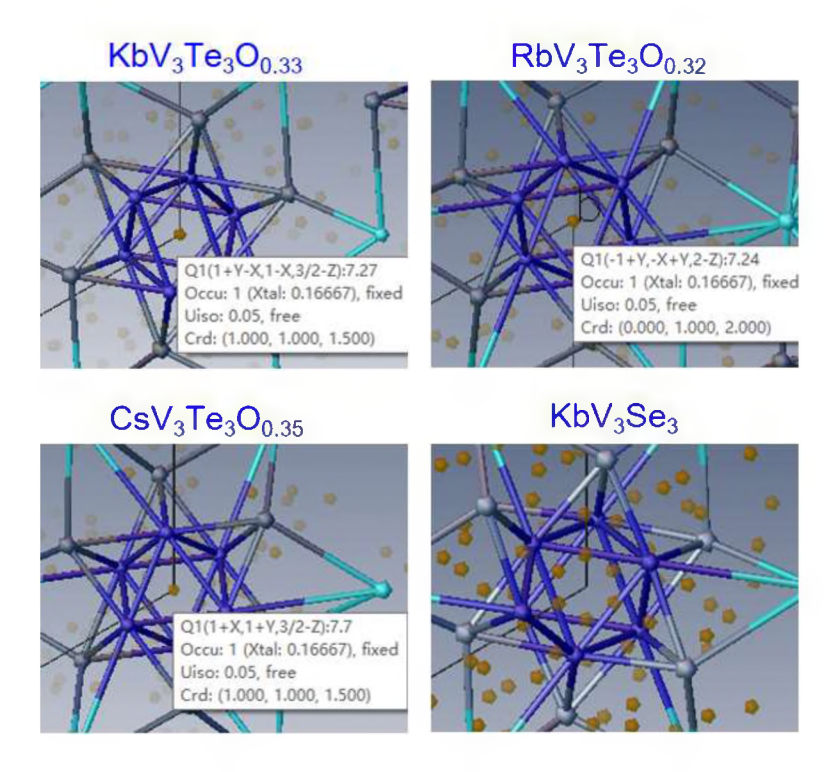


Figure S3. The scene for solving the structure of these V-based 133 phases with TlFe₃Te₃-type structure using Olex2 software: a residual peak \sim 7.5 Å is observed at the center of the V₆ octahedron in all three tellurides, while it is absent in KV₃Se₃. The brilliant blue, dark blue and gray spheres correspond to alkali metal, vanadium and chalcogen atoms, respectively.

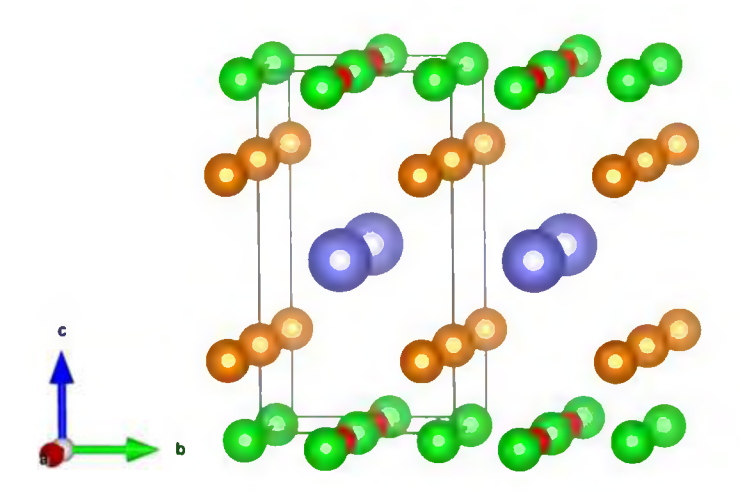


Figure S4. The structure of KV_2Se_2O refined from the SPXRD pattern with lattice parameters of a=3.97549(2) and c=7.3450(1) in P4/mmm space group. The light blue, green, dark yellow and red spheres correspond to K, V, Se, and O atoms, respectively.

In the KV₃Se₃ synchrotron powder X-ray diffraction pattern, an oxyselenide impurity KV₂Se₂O was observed. Based on our refinement, the crystal structure was determined as a tetragonal lattice with P4/mmm space group and lattice parameters of a=3.97549(2) and c=7.3450(1), as shown in Figure S4. KV₂Se₂O is isostructural with the reported RbV₂Te₂O and CsV₂S₂O, which are suggested to be bad metals. [1] [2]

Local structure

For investigating the local structure of KV₃Se₃ and KV₃Te₃O_{δ}, we performed synchrotron X-ray total scattering studies. The crystals obtained in this work are very malleable and are not easy to grind. We used polycrystalline samples for the scattering measurements. Based on the X-ray total scattering, we performed atomic pair distribution function (PDF) analyses which take the Fourier transform of the normalized diffraction pattern to generate the real space atomic correlation G(r) functions. PDFs were extracted from high energy synchrotron X-ray scattering by direct Fourier transform of the reduced structure function (F(Q), up to $Q \approx 23$ Å) using the 11-ID-B beam line at Advanced Photon Source (APS) of Argonne National Laboratory. The X-ray wavelength was 0.1430 Å. G(r) functions, $G(r) = 4\pi r [\rho(r) - \rho_o]$, where $\rho(r)$ and ρ_o are the local and average atomic number densities, were computed with PDFgetX2 software. The peak width is given by:

$$\sigma = \sigma' \sqrt{1 - \frac{\delta_1}{r} - Q_{broad}^2 r^2}$$

Here σ ' is the peak width without correction, given by the structural model; δ_1/r is the term that corrects the high temperature effects, and Q_{broad} is the apparatus induced width. The PDF profile refinements were carried out for the KV₃Se₃ and KV₃Te₃O_{δ} using PDFgui program. The structural model is refined in the different symmetries ($P6_3/m$, $P2_1/m$, $P2_1/c$ and $P2_1$). The parameters, including lattice constants, atomic position and anisotropic displacement parameters, are allowed to vary until a best-fit of the PDF is obtained using a least-squares approach. Fitting the transformed data shifts the fit to direct atom-atom spacing, rather than the crystallographic symmetry. Therefore, it allows for the modeling of the local structure through least-squares techniques. Given that PDF data can be treated as the assembly of snapshots of the instantaneous atomic arrangements, low and high r corresponds to the local structure and average structure, respectively.

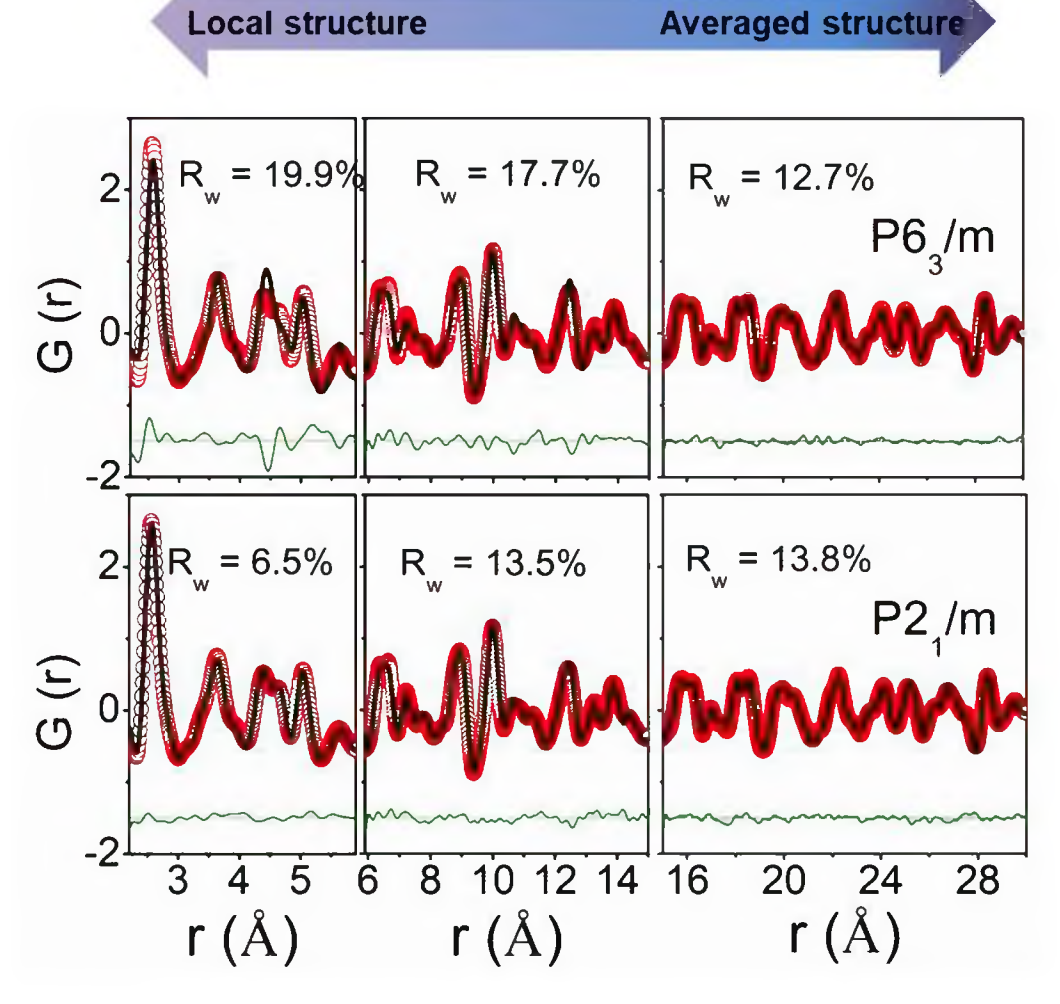


Figure S5. Fitting the PDF data at 300 K for KV₃Se₃ using $P6_3/m$ (up) and $P2_1/m$ model (below) in low r range (2.2-5.9 Å), middle r range (5.9-15 Å) and high r range (15-30 Å). It is very clear that the monoclinic $P2_1/m$ model shows better fit in the low r range, while the original hexagonal $P6_3/m$ models shows better fit in the high r range. The data indicate the distortion occurs locally.

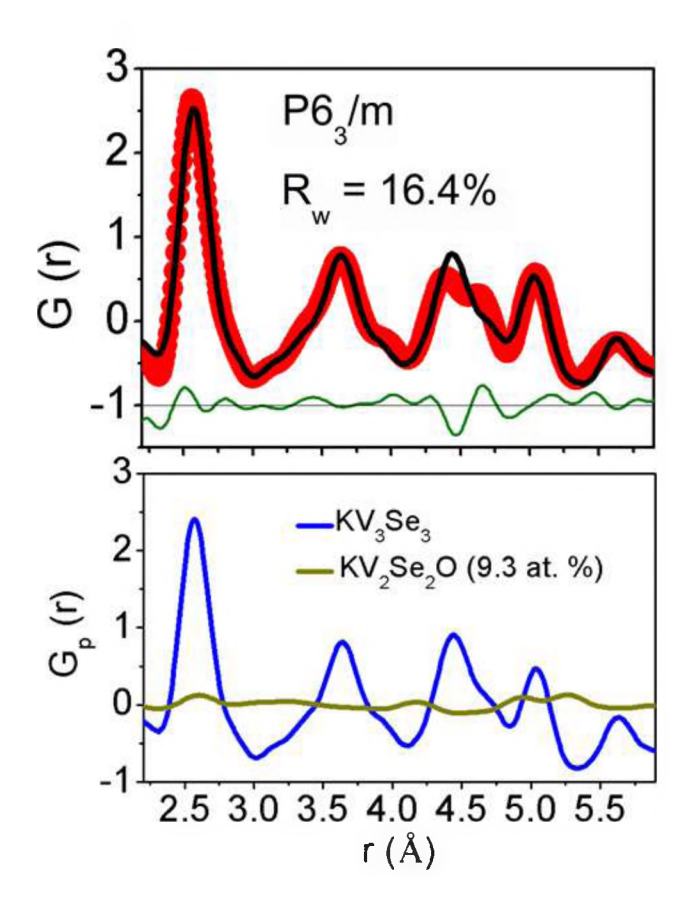


Figure S6. Fitting the KV₃Se₃ PDF data at 300 K in low r range (2.2-5.9 Å) using $P6_3/m$ model with KV₂Se₂O as the second phase.

We tried to add KV_2Se_2O as the second phase to refine the low-r PDF data for KV_3Se_3 . The concentration of KV_2Se_2O was fixed to be 9.3 at.% by constraining the scale factor when we refine the data using PDFgui. However, the presence of KV_2Se_2O only reduced the R_w value from 19.9% to 16.4%. Furthermore, the splitting peak located at ~4.5 Å, which is the main shortcoming of the $P6_3/m$ model, could not be fit by KV_2Se_2O as shown in Figure S6.

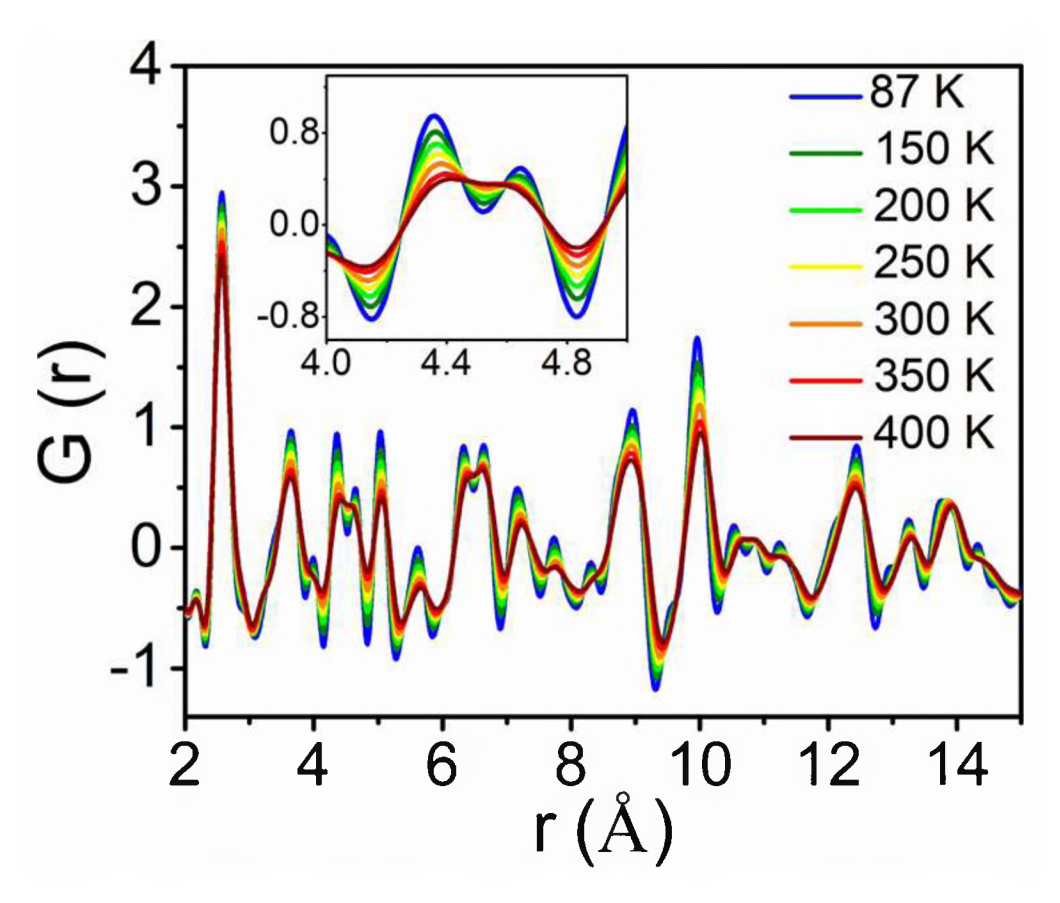


Figure S7. The variable temperature PDF data for KV_3Se_3 in low r range (2-15 Å) from 400 to 87 K. Inset shows the enlarged peak splitting at ~4.5 Å.

The temperature dependent PDF data for KV_3Se_3 show qualitatively similar behaviour from 400 to 87 K, indicating that no phase transition occurred in the measured temperature range. We noticed that the split PDF peak located at ~4.5 Å persists in the whole temperature range, implying that the distortion of the V triangle in the *ab* plane is retained to the lowest temperature measured.

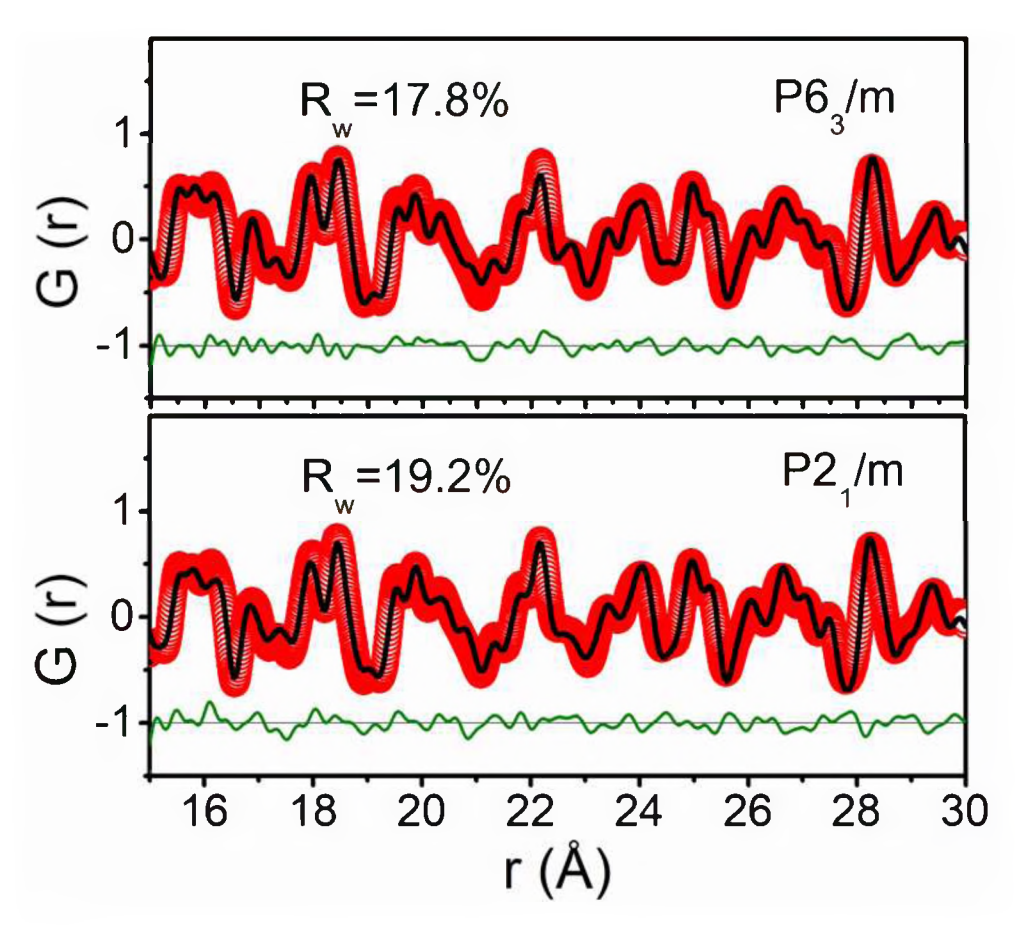


Figure S8. Fitting the PDF data at 87 K of KV₃Se₃ using $P6_3/m$ (up) and $P2_1/m$ model (below) in high r range (15-30 Å). The original hexagonal $P6_3/m$ models shows better fit in the high r range, indicating that the average low-range structure is still hexagonal $P6_3/m$ at 87 K.

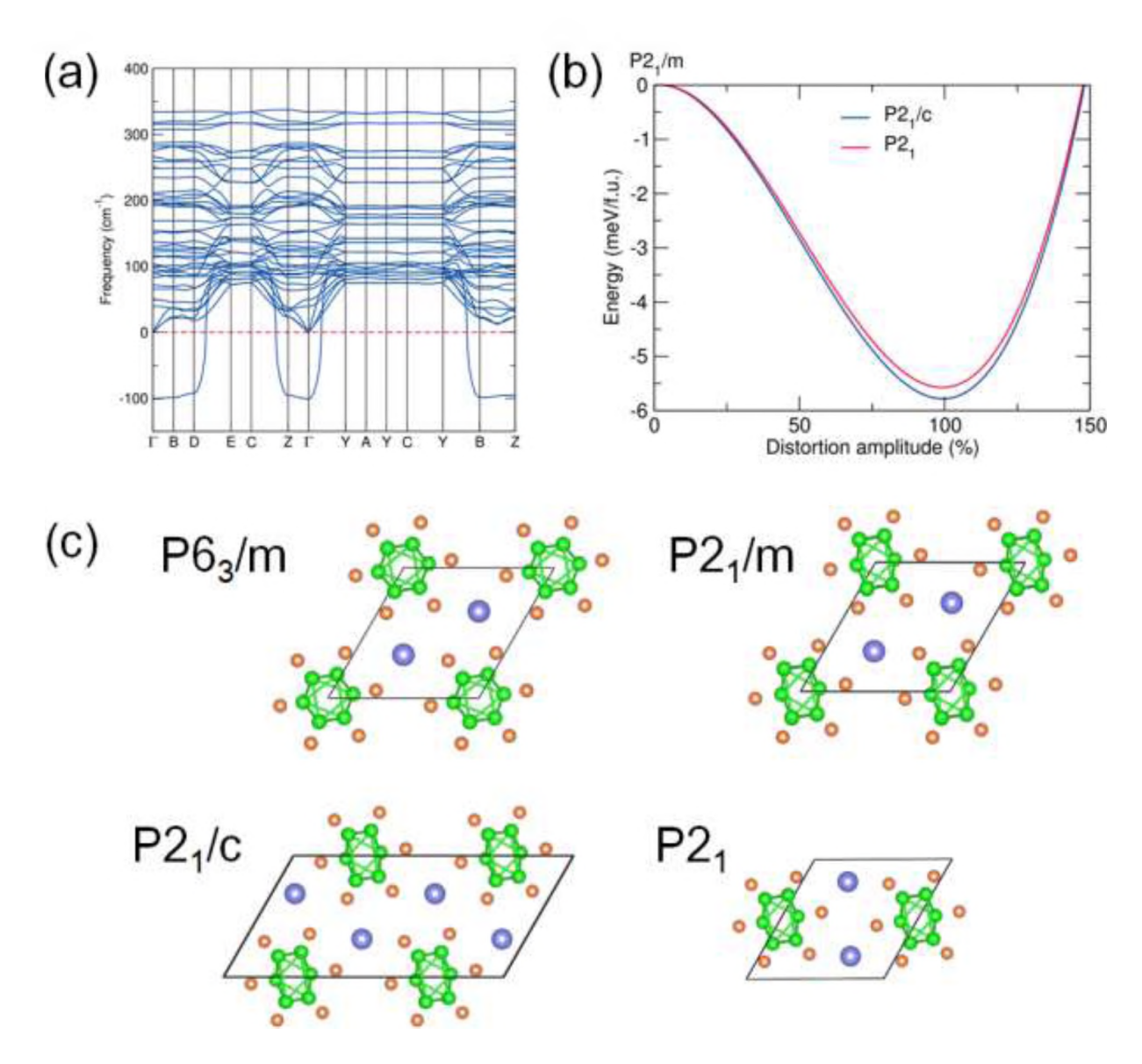


Figure S9. (a) Phonon dispersions of KV₃Se₃ with $P2_1/m$ symmetry. (b) Energy gain obtained by linear interpolation between the $P2_1/m$ and the $P2_1/c$ and $P2_1$ structures derived from the phonon instabilities. (c) View of these monoclinic structures along the chain direction.

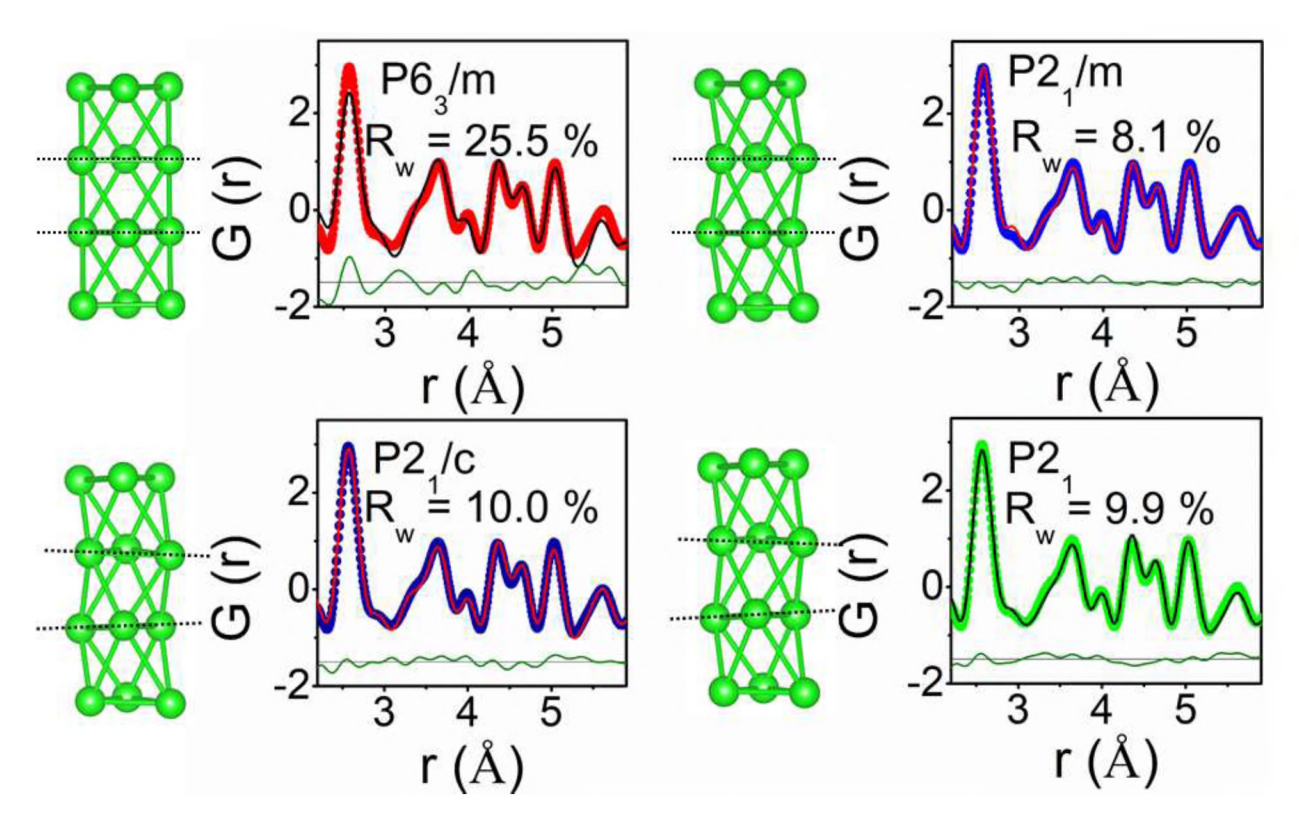


Figure S10. Fitting the PDF data of KV₃Se₃ over the low r range (2.2-5.9 Å) at 87 K with the $P6_3/m$, $P2_1/m$, $P2_1/c$ and $P2_1$ models. Details of the distortions are also depicted: the V triangle planes in $P2_1/m$ are parallel to each other, and the distortion only occurs in the ab plane. In $P2_1/c$ and $P2_1$, the V₆ octahedron further distort along the c direction.

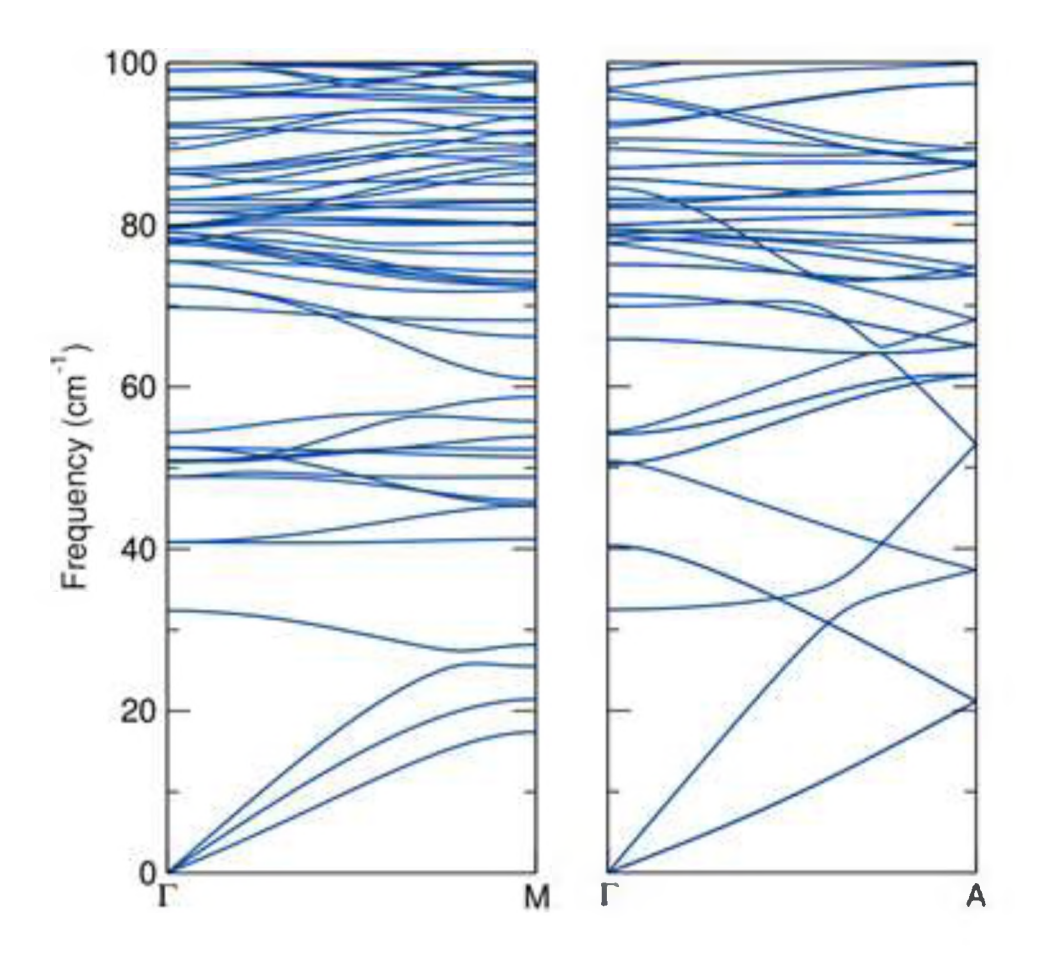


Figure S11. Phonon dispersions for the structural model with ordered oxygen atoms of $KV_3Te_3O_{0.33}$ ($P6_3/m$ symmetry), which after structural optimization exhibits out-of-plane distortions comprising a V_3 -triangle-trimerization along the chain direction. Phonon dispersions (left) orthogonal to and (right) parallel to the chain direction are all positive, indicating that unlike KV_3Se_3 the V_6 octahedra in $KV_3Te_3O_{0.33}$ are stable in the ab plane after the structural relaxation.

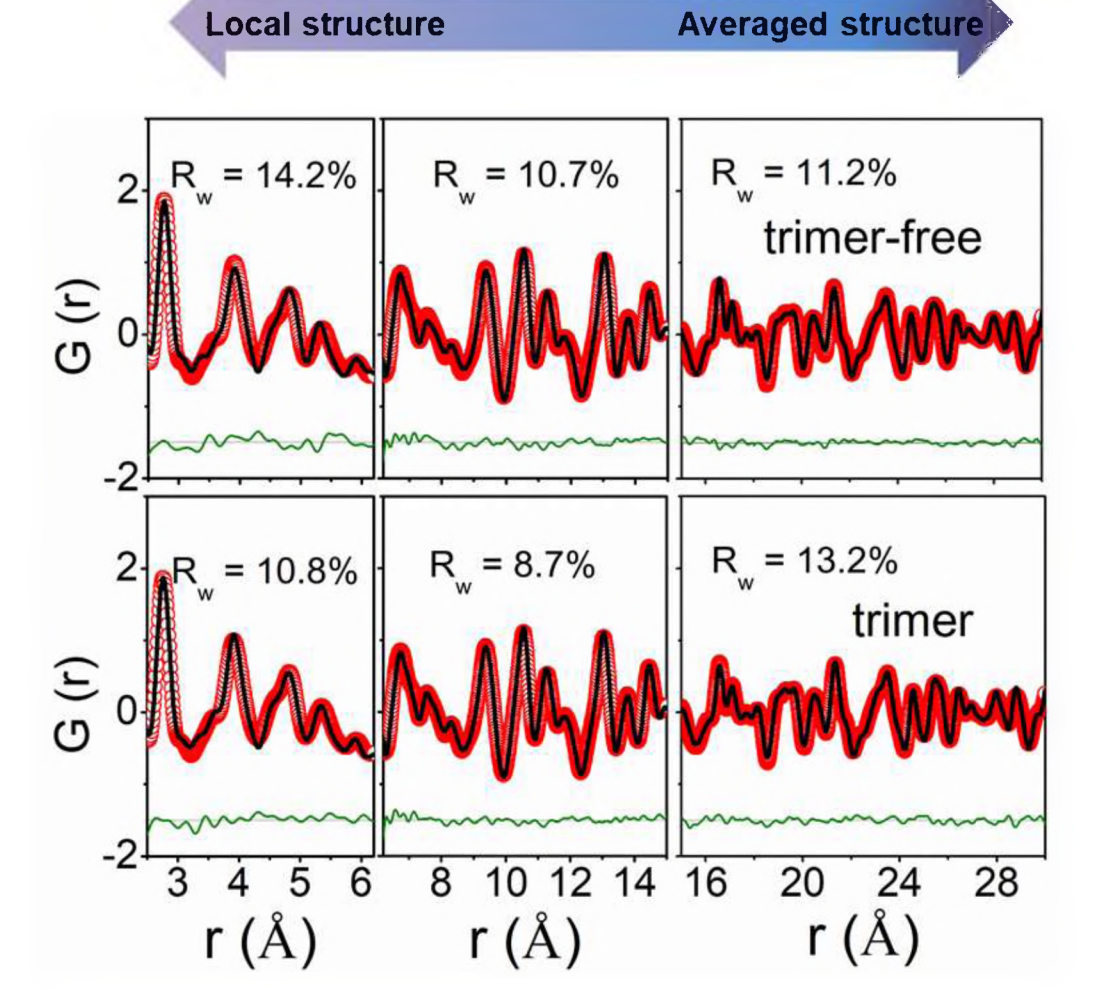
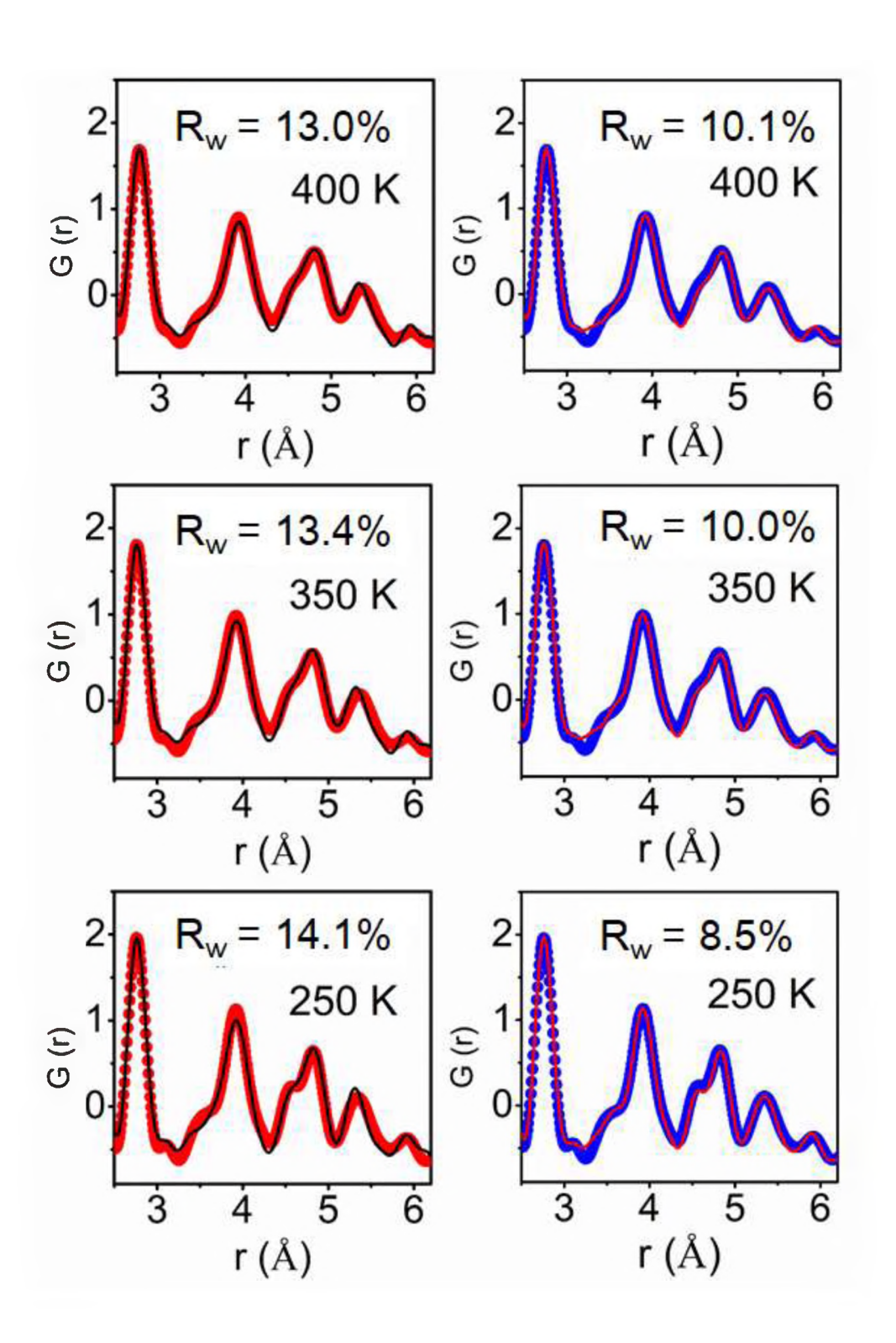


Figure S12. Fitting the PDF data at 300 K of $KV_3Te_3O_{0.33}$ using the trimer-free (upper) and trimer models (lower) in the low r range (2.5-6.2 Å), middle r range (6.2-15 Å) and high r range (15-30 Å). It is clear that the trimer model gives a better fit in the low r range, while the original trimer-free models provides a better fit in the high r range. This indicates the trimerization occurs locally and has a short coherence length.



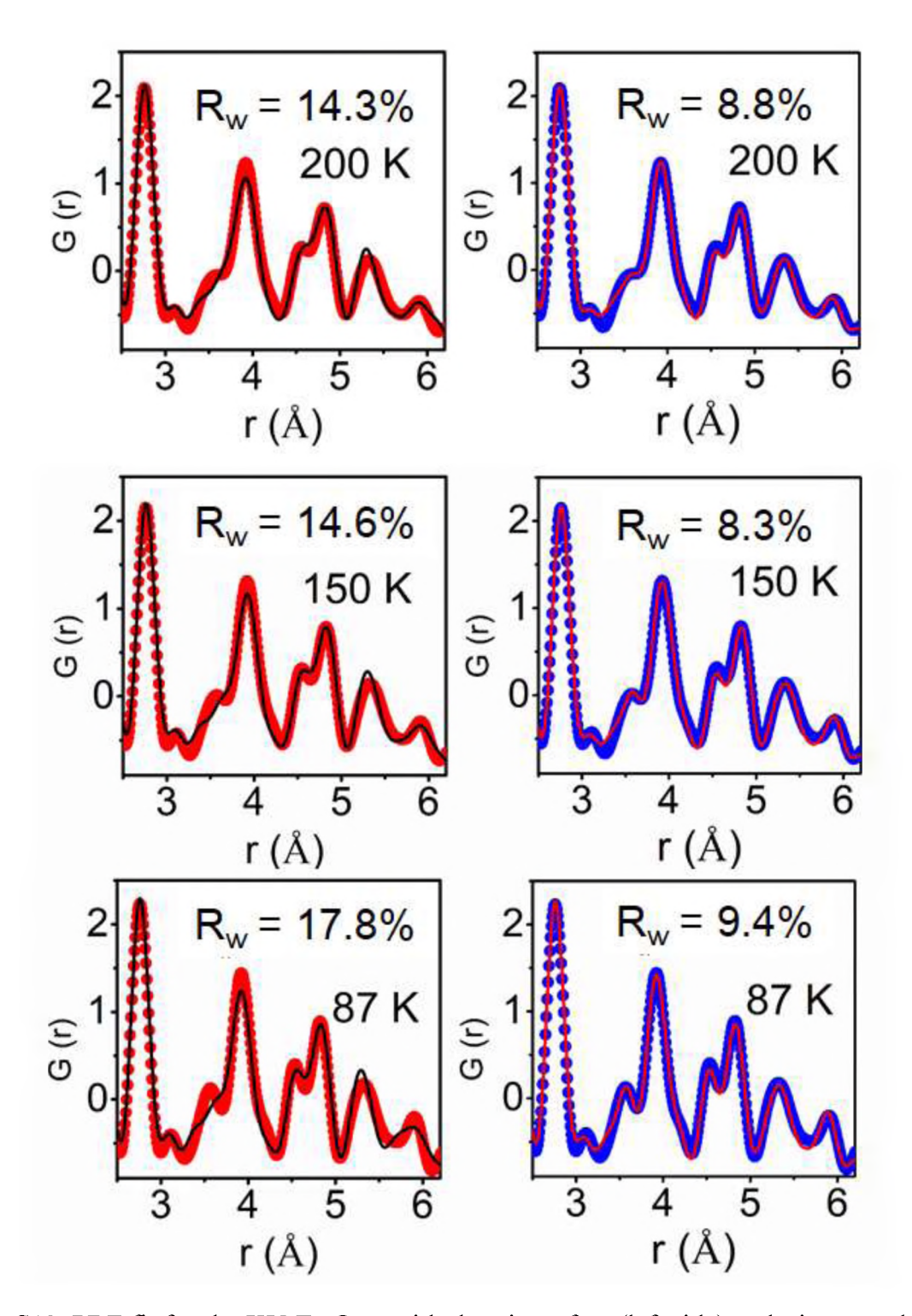


Figure S13. PDF fit for the KV₃Te₃O_{0.33} with the trimer-free (left side) and trimer model (right side) at low r range (2.5-6.2 Å) from 400 to 87 K. The red and blue circles correspond to the experimental data. The black and red lines correspond to the calculated data based on the structure models.

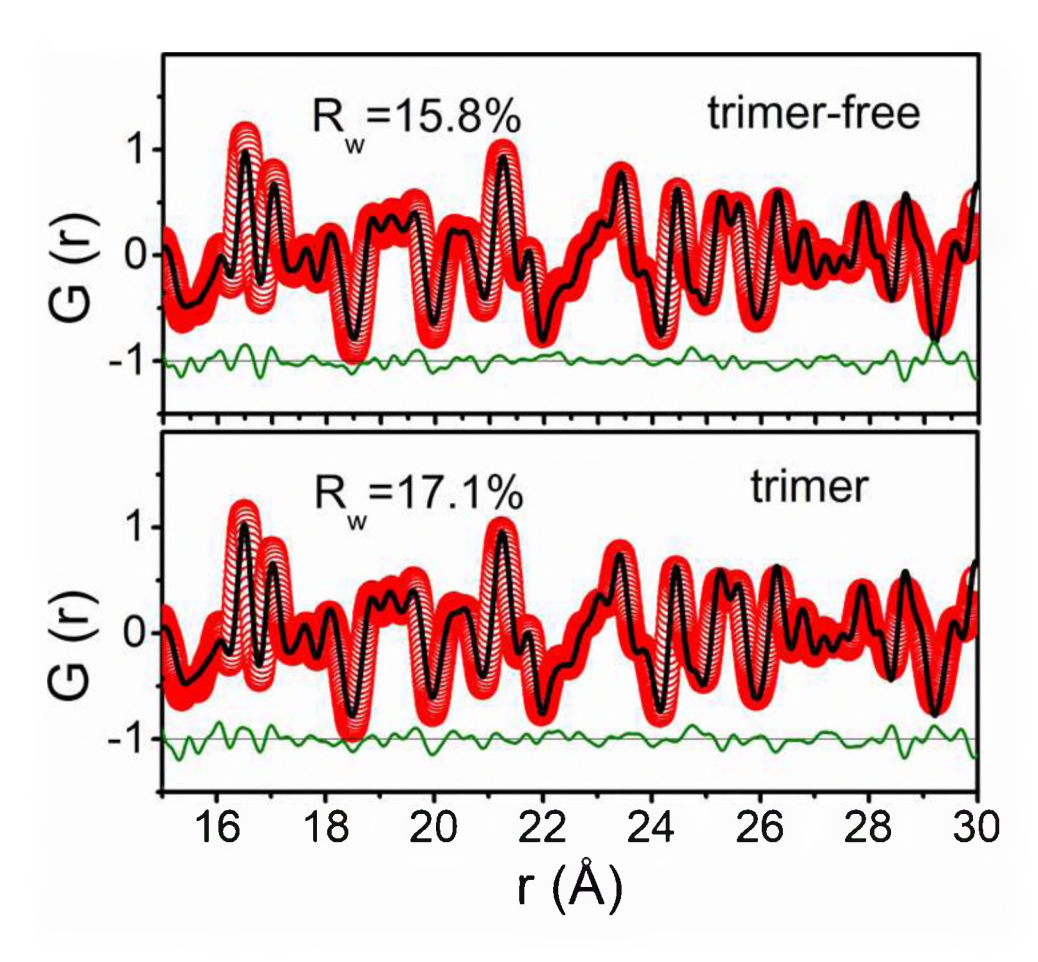


Figure S14. Fitting the PDF data at 87 K of $KV_3Te_3O_\delta$ using the trimer-free (upper) and trimer models (lower) in high r range (15-30 Å). The original trimer-free models shows better fit in the high r range, indicating that the average low-range structure is trimer-free at 87 K.

Physical Properties

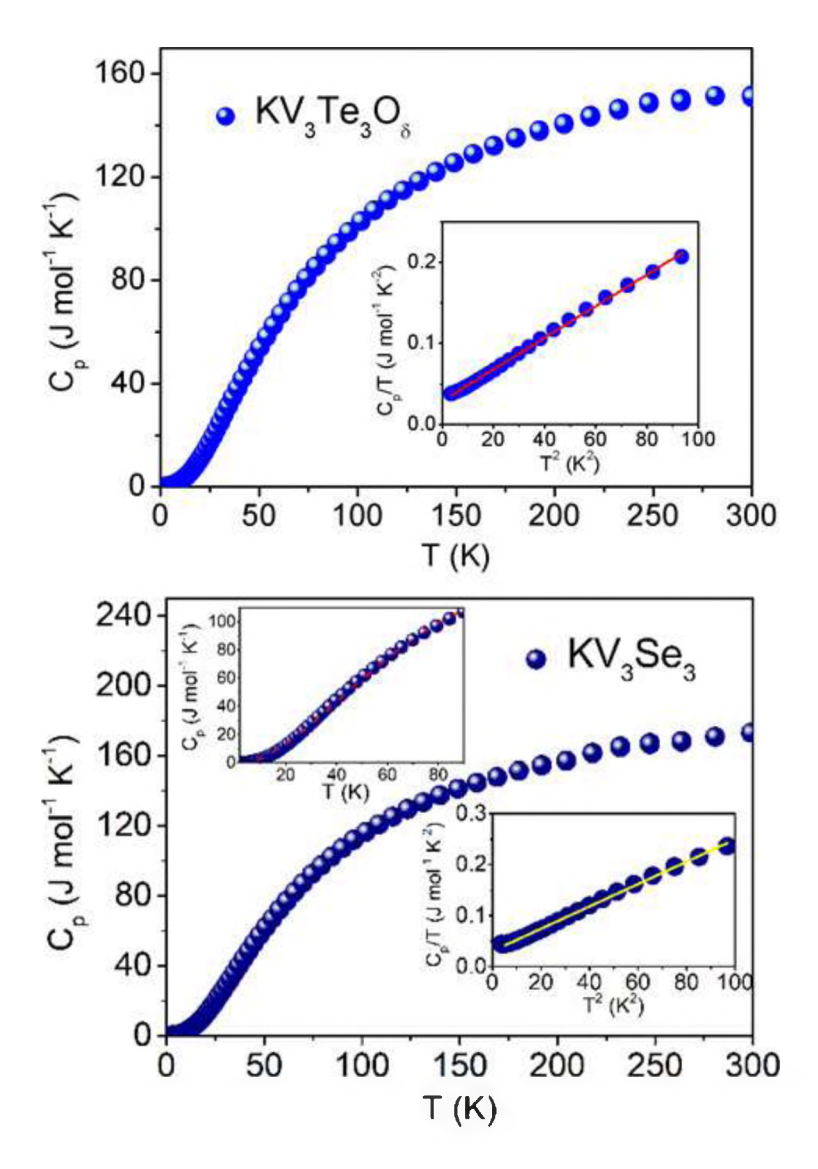


Figure S15. Temperature-dependent specific heat capacity of KV₃Te₃O_{0.33} (upper) and KV₃Se₃ (lower) measured from 300 to 2 K. Inset shows the data between 2-10 K which are fitted by the formula $C(T) = \gamma T + \beta T^3$.

As shown in Figure S15, according to $C_P = \gamma T + \beta T^3$, where γT and βT^3 are the electron and phonon conributions, the calculated coefficients are $\gamma = 0.02929$ J mol⁻¹ K⁻², and $\beta = 0.00195$ J mol⁻¹ K⁻⁴, respectively, for KV₃Te₃O_{0.33}. The Debye temperature (Θ_D) of KV₃Te₃O_{0.33}, calculated by $\Theta_D = (12\pi^4 \text{NR}/5\beta)^{1/3}$, is determined to be ~192 K. For KV₃Se₃, $\gamma = 0.03036$ J mol⁻¹ K⁻², $\beta = 0.00219$ J mol⁻¹ K⁻⁴, and $\Theta_D = \sim 184$ K.

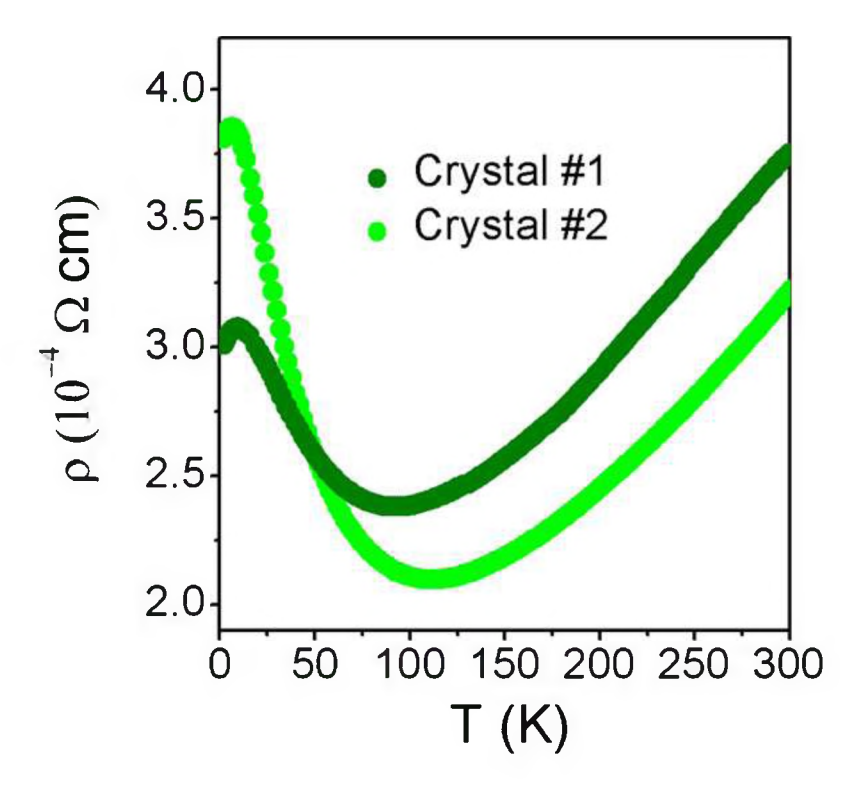


Figure S16. Resistivity vs temperature of two different $CsV_3Te_3O_\delta$ crystals from the same batch. The curve of sample #1 is used in the main text.

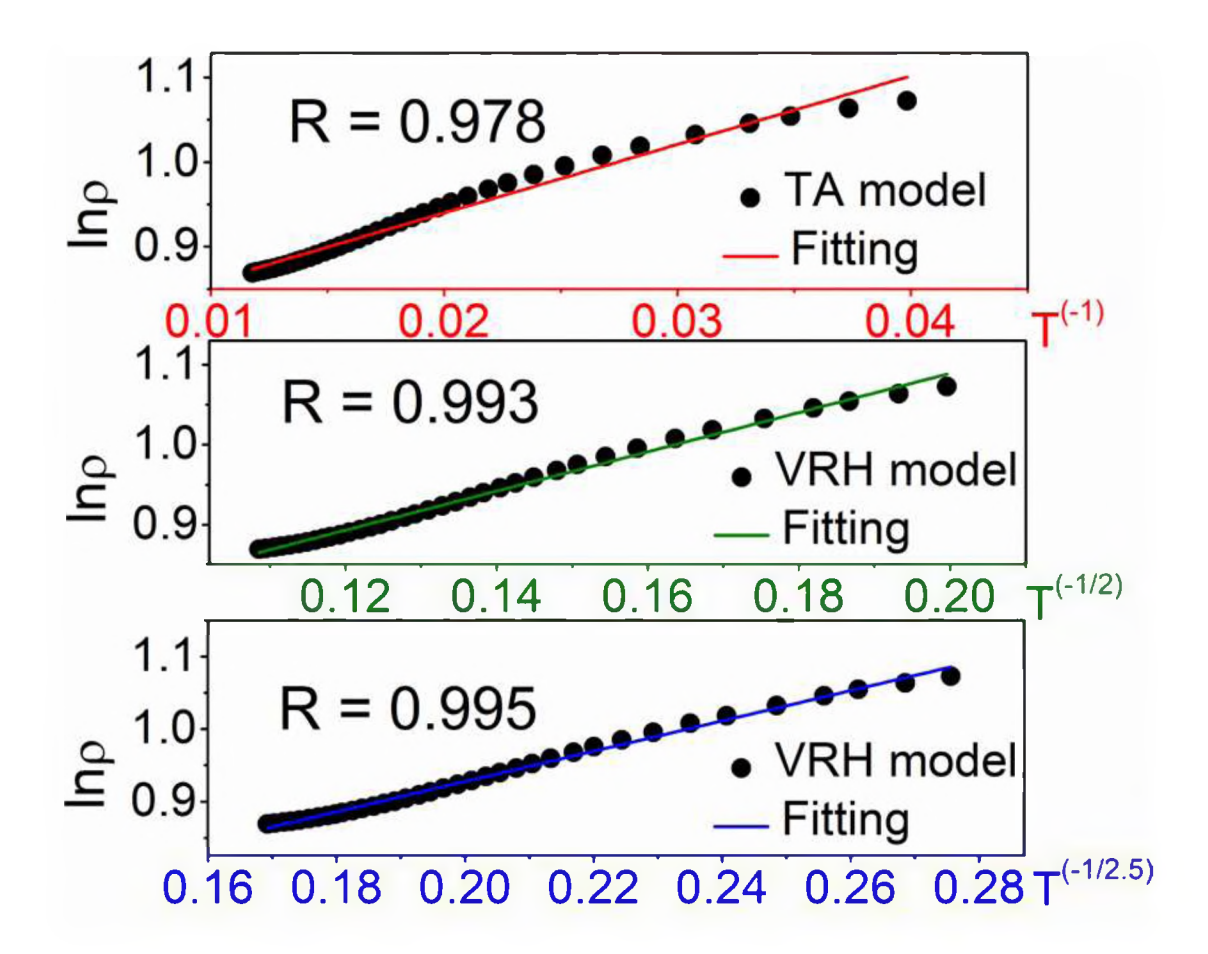


Figure S17. Fitting the resistivity data of $CsV_3Te_3O_{0.32}$ (sample #1) from 50 to 100 K with variable range hopping (VRH) and thermal activation (TA) models.

A conventional semiconductor, which has an energy gap in the density-of-states will exhibit thermal activated (TA) transport following an Arrhenius equation:

$$\rho \propto e^{E_g/k_BT}$$

In contrast, for a strongly disordered electron system, charge transport occurs by hopping between nearby localized states. This results in a variable range hopping model (VRH):

$$\rho(T) = \rho_0 \exp\left[(T_0/T)^{\frac{1}{1+d}} \right],$$

where T_0 is the effective localization temperature describing both the hopping length and activation energy, and d is the dimensionality of the system.

For CsV₃Te₃O_{0.32}, the VRH model is better than the TA fit to the resistivity data, indicating the semiconducting behavior in the telluride crystals. We find that by using d = 1.5, the fitting is

improved compared with d = 1. This is in agreement with transport consisting of disordered chain conduction.^[3]

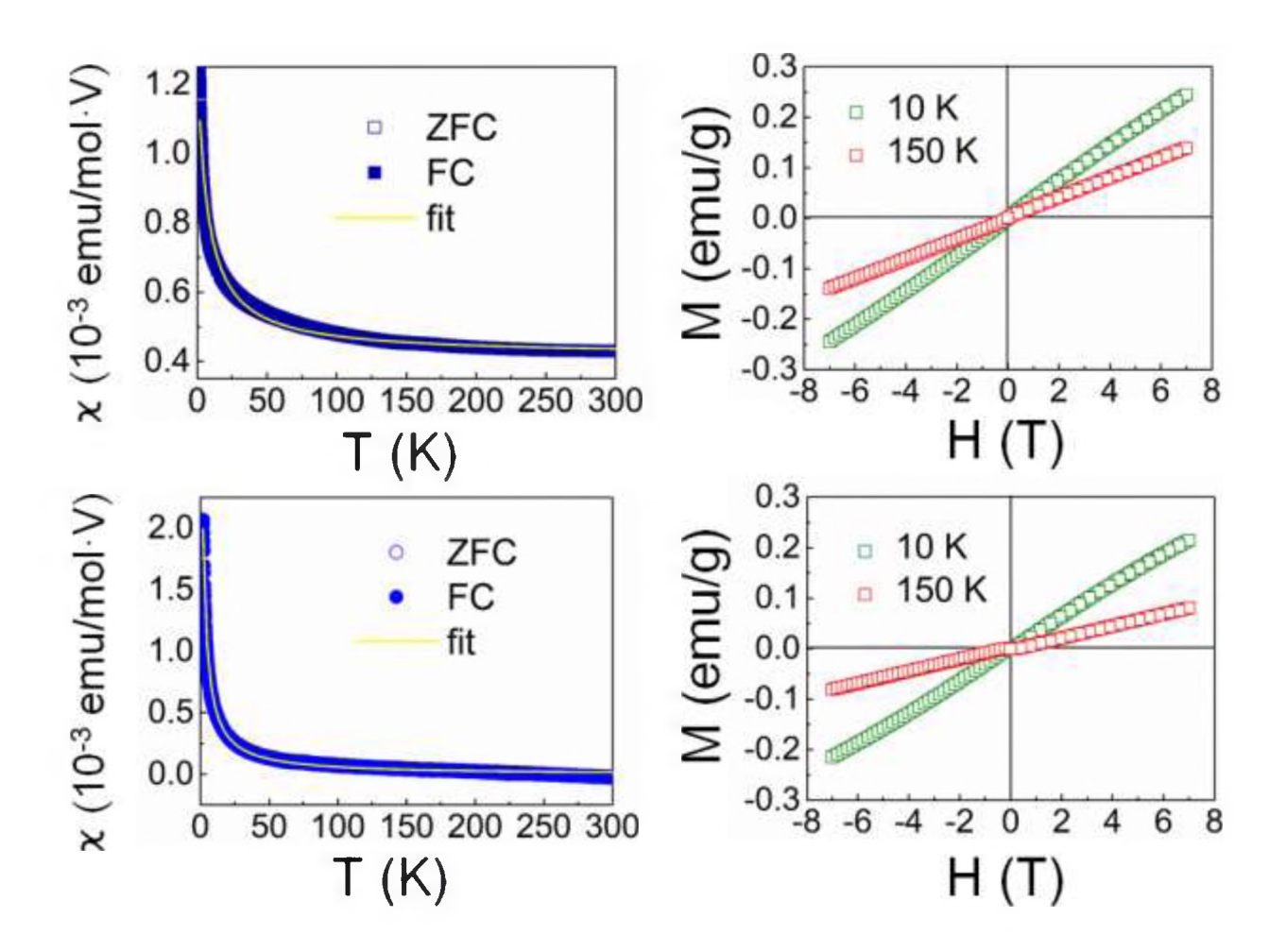


Figure S18. Temperature dependence with the field H = 1000 Oe and field dependence at 10 and 150 K of the magnetic susceptibility for KV_3Se_3 (up) and $KV_3Te_3O_\delta$ (below). The yellow lines are the fitting results by using Curie-Weiss law.

Both temperature-dependent magnetization curves are fit by the Curie-Weiss law:

$$x = x_0 + \frac{C}{T - \theta}$$

where χ_0 is the temperature-independent term, C the Curie constant and θ the paramagnetic Curie temperature. The effective moments were calculated using the equation: $\mu_{eff} = \sqrt{8C}\mu_B$.

The obtained small effective magnetic of V in these Q1D materials are comparable to the values in ACr_3As_3 and ANi_3Se_3 .^{[4] [5] [6] [7]}

Theoretical electronic structures

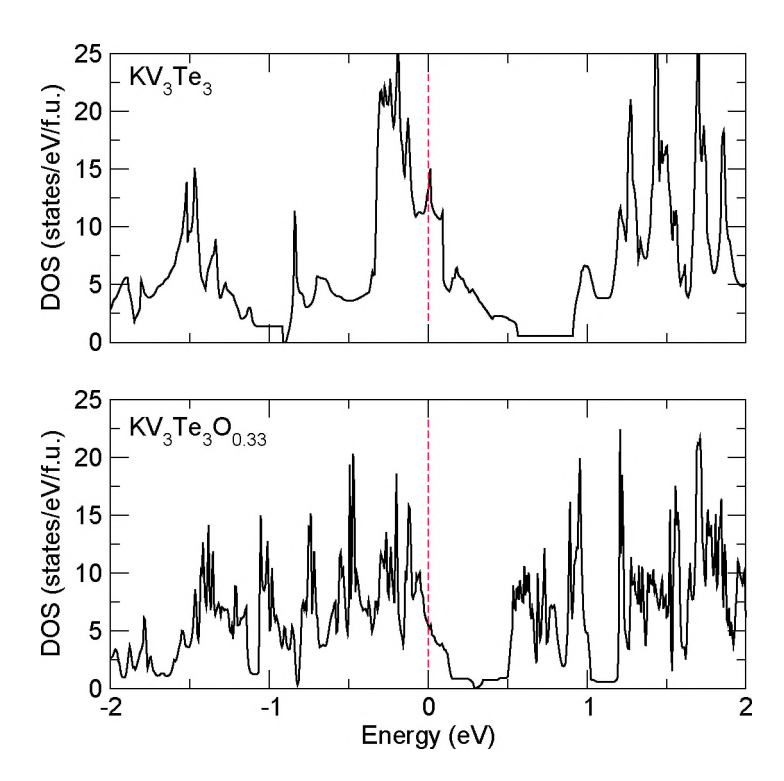


Figure S19. Total DOS of hexagonal hypothetical "empty" KV₃Te₃ and KV₃Te₃O_{0.33}. The Fermi level is at 0 eV (dashed line).

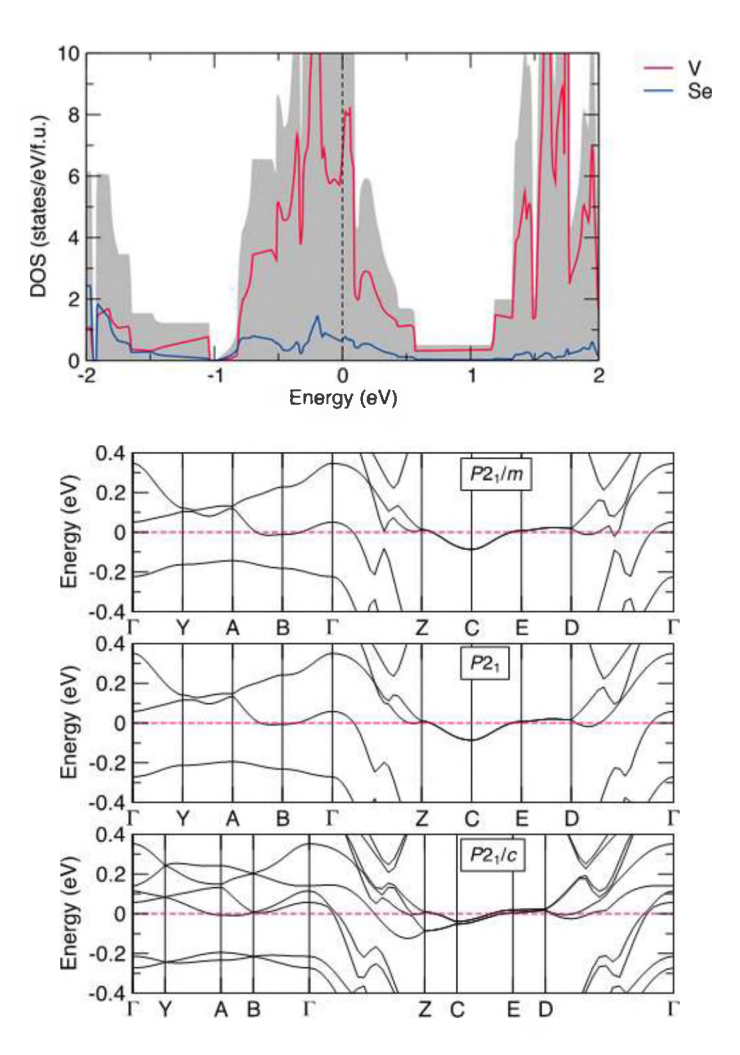


Figure S20. Total and partial density of states (DOS) of hexagonal KV₃Se₃ with the original $P6_3/m$ structure and electronic band structure for the distorted $P2_1/m$, $P2_1$, and $P2_1/c$ phases.

Table 1. Crystal data and structure refinement for KV_3Se_3 at 293(2) K.

Empirical formula	KV_3Se_3
Formula weight	428.79
Temperature	293(2) K
Wavelength	0.71073 Å
Crystal system	Hexagonal
Space group	P6 ₃ /m
	$a = 9.0066(5) \text{ Å}, \alpha = 90^{\circ}$
Unit cell dimensions	$b = 9.0066(5) \text{ Å}, \beta = 90^{\circ}$
	$c = 4.3599(2) \text{ Å}, \gamma = 120^{\circ}$
Volume	$306.29(4) \text{ Å}^3$
Z	2
Density (calculated)	4.649 g/cm^3
Absorption coefficient	22.841 mm ⁻¹
F(000)	380
Crystal size	$0.055 \times 0.061 \times 1 \text{ mm}^3$
θ range for data collection	4.526 to 28.262°
Index ranges	-12<=h<=10, -11<=k<=11, -5<=l<=5
Reflections collected	2259
Independent reflections	$284 [R_{int} = 0.0641]$
Completeness to $\theta = 25.242^{\circ}$	99.1%
Refinement method	Full-matrix least-squares on F ²
Data / restraints / parameters	284 / 0 / 16
Goodness-of-fit	1.285
Final R indices $[I > 2\sigma(I)]$	$R_{obs} = 0.1198$, $wR_{obs} = 0.2838$
R indices [all data]	$R_{all} = 0.1198, wR_{all} = 0.2838$
Largest diff. peak and hole	5.838 and -5.920 e·Å ⁻³
$R = \sum F_0 - F_0 / \sum F_0 wR = \{\sum w(F_0 ^2 - F_0 ^2)^2\} $	$\sqrt{\sum [w(E_* ^4)]^{\frac{1}{2}}}$ and $w=1/[\sigma^2(E_0^2)+94.5503D]$

 $R = \Sigma ||F_o| - |F_c|| / \Sigma |F_o|, \ wR = \{\Sigma [w(|F_o|^2 - |F_c|^2)^2] / \Sigma [w(|F_o|^4)]\}^{1/2} \ and \ w = 1/[\sigma^2(Fo^2) + 94.5503P]$ where $P = (Fo^2 + 2Fc^2)/3$

Table 2. Atomic coordinates ($\times 10^4$) and equivalent isotropic displacement parameters ($\mathring{A}^2 \times 10^3$) for KV₃Se₃ at 293(2) K with estimated standard deviations in parentheses

.

Label	X	У	z	Occupancy	U _{eq} *
Se	2917(5)	9400(5)	2500	1	12(1)
V	1882(13)	11557(12)	2500	1	30(2)
K	6667	13333	2500	1	27(4)

^{*}U_{eq} is defined as one third of the trace of the orthogonalized U_{ij} tensor.

Table 3. Anisotropic displacement parameters ($Å^2 \times 10^3$) for KV₃Se₃ at 293(2) K with estimated standard deviations in parentheses.

Label	U ₁₁	U_{22}	U ₃₃	U_{12}	U_{13}	U_{23}	
Se	13(2)	12(2)	11(2)	7(2)	0	0	
V	69(6)	47(5)	7(3)	55(5)	0	0	
K	26(5)	26(5)	29(9)	13(2)	0	0	

The anisotropic displacement factor exponent takes the form: $-2\pi^2[h^2a^{*2}U_{11} + ... + 2hka^*b^*U_{12}]$.

Table 4. Crystal data and structure refinement for $KV_3Te_3O_{0.33}$ at 293(2) K.

Empirical formula	KV ₃ Te ₃ O _{0.33}
Formula weight	579.99
Temperature	273.15 K
Wavelength	0.71073 Å
Crystal system	Hexagonal
Space group	P6 ₃ /m
	$a = 9.6615(5) \text{ Å}, \alpha = 90^{\circ}$
Unit cell dimensions	$b = 9.6615(5) \text{ Å}, \beta = 90^{\circ}$
	$c = 4.5069(2) \text{ Å}, \gamma = 120^{\circ}$
Volume	$364.33(4) \text{ Å}^3$
Z	2
Density (calculated)	5.287 g/cm^3
Absorption coefficient	15.997 mm ⁻¹
F(000)	493
Crystal size	0.028 x 0.023 x 0.305 mm ³
θ range for data collection	2.434 to 28.235°
Index ranges	-12<=h<=12, -12<=k<=12, -5<=l<=6
Reflections collected	4106
Independent reflections	$337 [R_{int} = 0.0272]$
Completeness to $\theta = 25.242^{\circ}$	99.2%
Refinement method	Full-matrix least-squares on F ²
Data / restraints / parameters	337 / 0 / 17
Goodness-of-fit	1.329
Final R indices $[I > 2\sigma(I)]$	$R_{obs} = 0.0158$, $wR_{obs} = 0.0403$
R indices [all data]	$R_{all} = 0.0160, wR_{all} = 0.0404$
Largest diff. peak and hole	0.616 and -1.390 e·Å ⁻³

 $R = \Sigma ||F_o| - |F_c|| / \Sigma |F_o|, \text{ wR} = \{\Sigma [w(|F_o|^2 - |F_c|^2)^2] / \Sigma [w(|F_o|^4)]\}^{1/2} \text{ and }$ w=1/[\sigma^2(Fo^2)+(0.0209P)^2+0.4049P] where P=(Fo^2+2Fc^2)/3

Table 5. Atomic coordinates ($\times 10^4$) and equivalent isotropic displacement parameters ($\mathring{A}^2 \times 10^3$) for KV₃Te₃O_{0.33} at 293(2) K with estimated standard deviations in parentheses.

Label	X	у	Z	Occupancy	U _{eq} *
Te(1)	3614(1)	2980(1)	2500	1	11(1)
V(2)	330(1)	1813(1)	2500	1	9(1)
K(4)	3333	6667	2500	1	22(1)
O(1)	0	0	0	0.33(2)	3(4)

^{*}U_{eq} is defined as one third of the trace of the orthogonalized U_{ij} tensor.

Table 6. Anisotropic displacement parameters ($Å^2 \times 10^3$) for KV₃Te₃O_{0.33} at 293(2) K with estimated standard deviations in parentheses.

Label	U_{11}	U_{22}	U_{33}	U_{12}	U_{13}	U_{23}	
Te	9(1)	12(1)	9(1)	3(1)	0	0	
V	9(1)	8(1)	8(1)	4(1)	0	0	
K	22(1)	22(1)	22(1)	11(1)	0	0	

The anisotropic displacement factor exponent takes the form: $-2\pi^2[h^2a^{*2}U_{11} + ... + 2hka^*b^*U_{12}]$.

Table 7. Crystal data and structure refinement for RbV₃Te₃O_{0.32} at 293(2) K

Empirical formula	RbV ₃ Te ₃ O _{0.32}
Formula weight	626.20
Temperature	293(2) K
Wavelength	0.71073 Å
Crystal system	Hexagonal
Space group	P6 ₃ /m
	$a = 9.8700(5) \text{ Å}, \alpha = 90^{\circ}$
Unit cell dimensions	$b = 9.8700(5) \text{ Å}, \beta = 90^{\circ}$
	$c = 4.5094(2) \text{ Å}, \gamma = 120^{\circ}$
Volume	$380.44(4) \text{ Å}^3$
Z	2
Density (calculated)	5.467 g/cm^3
Absorption coefficient	21.129 mm ⁻¹
F(000)	529
Crystal size	$0.082 \times 0.054 \times 0.698 \text{ mm}^3$
θ range for data collection	2.383 to 28.218°
Index ranges	-13<=h<=13, -13<=k<=13, -6<=l<=5
Reflections collected	4053
Independent reflections	$348 [R_{int} = 0.0295]$
Completeness to $\theta = 25.242^{\circ}$	97.7%
Refinement method	Full-matrix least-squares on F ²
Data / restraints / parameters	348 / 0 / 17
Goodness-of-fit	1.327
Final R indices $[I > 2\sigma(I)]$	$R_{obs} = 0.0167, wR_{obs} = 0.0405$
R indices [all data]	$R_{all} = 0.0167, wR_{all} = 0.0405$
Largest diff. peak and hole	0.951 and -1.552 e·Å ⁻³

 $R = \Sigma ||F_o| - |F_c|| / \Sigma |F_o|, \ wR = \{\Sigma [w(|F_o|^2 - |F_c|^2)^2] / \Sigma [w(|F_o|^4)]\}^{1/2} \ and \\ w = 1/[\sigma^2 (Fo^2) + (0.0155P)^2 + 0.9385P] \ where \ P = (Fo^2 + 2Fc^2)/3$

Table 8. Atomic coordinates ($\times 10^4$) and equivalent isotropic displacement parameters ($\mathring{A}^2 \times 10^3$) for RbV₃Te₃O_{0.32}at 293(2) K with estimated standard deviations in parentheses.

Label	X	У	Z	Occupancy	U _{eq} *
Те	3510(1)	2966(1)	2500	1	10(1)
Rb	3333	6667	2500	1	20(1)
V	279(1)	1761(1)	2500	1	8(1)
O	0	0	0	0.32(2)	3(4)

^{*}U_{eq} is defined as one third of the trace of the orthogonalized U_{ij} tensor.

Table 9. Anisotropic displacement parameters ($Å^2 \times 10^3$) for RbV₃Te₃O_{0.32} at 293(2) K with estimated standard deviations in parentheses.

Label	U_{11}	U_{22}	U ₃₃	U_{12}	U_{13}	U_{23}	
Те	14(1)	10(1)	9(1)	8(1)	0	0	
Rb	18(1)	18(1)	22(1)	9(1)	0	0	
V	7(1)	7(1)	9(1)	3(1)	0	0	

The anisotropic displacement factor exponent takes the form: $-2\pi^2[h^2a^{*2}U_{11} + ... + 2hka^*b^*U_{12}]$.

Table 10. Crystal data and structure refinement for $CsV_3Te_3O_{0.35}$ at 293(2) K.

$CsV_3Te_3O_{0.35}$
674.12
293(2) K
0.71073 Å
Hexagonal
P6 ₃ /m
$a = 10.1431(9) \text{ Å}, \alpha = 90^{\circ}$
$b = 10.143 \text{ Å}, \beta = 90^{\circ}$
$c = 4.4919(4) \text{ Å}, \gamma = 120^{\circ}$
400.22(8) Å ³
2
5.594 g/cm^3
18.525 mm ⁻¹
566
$0.6 \times 0.042 \times 0.054 \text{ mm}^3$
2.319 to 28.310°
-13<=h<=13, -13<=k<=13, -5<=l<=5
2841
$367 [R_{int} = 0.0232]$
96.8%
Full-matrix least-squares on F ²
367 / 0 / 18
1.258
$R_{\rm obs} = 0.0165, WR_{\rm obs} = 0.0430$
$R_{all} = 0.0170, WR_{all} = 0.0433$
1.118 and -0.743 e·Å ⁻³

 $R = \Sigma ||F_o| - |F_c|| / \Sigma |F_o|, \text{ wR} = \{\Sigma [w(|F_o|^2 - |F_c|^2)^2] / \Sigma [w(|F_o|^4)]\}^{1/2} \text{ and }$ $w = 1/[\sigma^2(Fo^2) + (0.0212P)^2 + 1.0740P] \text{ where } P = (Fo^2 + 2Fc^2)/3$

Table 11. Atomic coordinates ($\times 10^4$) and equivalent isotropic displacement parameters ($\mathring{A}^2 \times 10^3$) for CsV₃Te₃O_{0.35} at 293(2) K with estimated standard deviations in parentheses.

Label	X	у	Z	Occupancy	U _{eq} *
Te(1)	3389(1)	465(1)	2500	1	11(1)
Cs(2)	3333	-3333	2500	1	20(1)
V(3)	229(1)	-1458(1)	2500	1	9(1)
O(1)	0	0	0	0.35(2)	2(4)

^{*}U_{eq} is defined as one third of the trace of the orthogonalized U_{ij} tensor.

Table 12. Anisotropic displacement parameters ($Å^2 \times 10^3$) for CsV₃Te₃O_{0.35} at 293(2) K with estimated standard deviations in parentheses.

Label	U_{11}	U_{22}	U ₃₃	U_{12}	U_{13}	U_{23}	
Te(1)	10(1)	15(1)	9(1)	7(1)	0	0	
Cs(2)	19(1)	19(1)	23(1)	9(1)	0	0	
V(3)	9(1)	9(1)	8(1)	5(1)	0	0	

The anisotropic displacement factor exponent takes the form: $-2\pi^2[h^2a^{*2}U_{11} + ... + 2hka^*b^*U_{12}]$.

Table S13. Crystallographic data of KV_3Se_3 obtained from the structural refinement of synchrotron powder X-ray diffraction at room temperature, including atomic coordinates ($\times 10^4$) and equivalent isotropic displacement parameters ($\mathring{A}^2 \times 10^3$).

Chemical formula	KV ₃ Se ₃
Crystal system	Hexagonal
Space group	<i>P</i> 6 ₃ / <i>m</i> (No. 176)
Radiation type	Μο Κα
Wavelength (Å)	0.45785
2θ range (°)	0.5-30
a (Å)	9.0214(1)
c (Å)	4.3621(1)
$V(Å^3)$	307.454(2)
Z	2
R_{wp}	10.4%
χ^2	2.52
Atom x	z Occu. $U_{iso}(Å^2)$

Atom	x	У	Z	Occu.	$U_{\rm iso}({\rm \AA}^2)$
K	6667	3333	2500	1	23(1)
V	1854(1)	1529(1)	2500	1	28(1)
Se	2933(1)	9416(1)	2500	1	17(1)

Table S14. Crystallographic data of $KV_3Te_3O_\delta$ obtained from the structural refinement of synchrotron powder X-ray diffraction at room temperature, including atomic coordinates (×10⁴) and equivalent isotropic displacement parameters (Å²×10³).

Chemical formula			KV ₃ Te ₃ O _{0.14}				
Crystal system			Hexagonal				
Space group			$P6_3/m$ (No. 176)				
Radiation type			Μο Κα	Μο Κα			
Wavelength (Å)			0.45785				
2θ range (°)			0.5-30				
a (Å)			9.5982(1)	9.5982(1)			
c (Å)			4.5247(1)				
$V(Å^3)$			360.992(4)				
Z			2				
R_{wp}			11.6%				
χ2			5.74				
Atom	x	У	Z	Occu.	$U_{\rm iso}({\rm \AA}^2)$		
K	6667	3333	2500	1	30(1)		
V	1854(1)	1529(1)	2500	1	11(1)		
Te	2933(1)	9416(1)	2500	1	14(1)		
O	0	0	0	0.14(1)	3(1)		

Table S15. The atomic coordinates ($\times 10^5$) of the relaxed structure of KV₃Se₃ based on our DFT calculations.

Space group	Atom	X	у	Z
P2 ₁ /m	K	31383	75000	66621
	V1	2426	75000	88638
	V2	20454	25000	4519
	V3	17250	75000	19625
	Sel	64503	25000	93987
	Se2	29294	25000	35477
	Se3	5564	25000	72643
P2 ₁ /c	K	31355	74366	8305
	V1	2459	74539	19306
	V2	20433	23045	27295
	V3	17229	76116	34787
	Sel	35512	73545	28034
	Se2	29243	25624	42742
	Se3	5620	24583	11338
P2 ₁	K	18647	75185	33390
	V1	47545	74933	11389
	V2	70434	73457	4588
	V3	67230	26475	19574
	Sel	85508	23957	6061
	Se2	79249	75978	35485
	Se3	44385	25017	27326

Table S16. The atomic coordinates ($\times 10^5$) of the relaxed structure of KV₃Te₃O_{0.33} based on our DFT calculations.

Space group	Atom	X	у	Z
P6 ₃ /m	K 1	66667	33333	25000
	K2	33333	66667	8222
	V1	16295	13302	25000
	V2	3244	17629	8740
	Te1	6278	35466	25000
	Te2	35531	29286	8130
	O	0	0	0

Reference

- [1] Vallodr, M.; Merz, P.; Prots, Y.; Schelle, W. Bad-Metal-Layered Sulfide Oxide CsV₂S₂O, *Eur, J, Inorg. Chem*, 2016, 23-27.
- [2] Ablimit, A.; Sun, Y.-L.; Jiang, H.; Wu, S.-Q.; Liu, Y.-B.; Cao, G.-H. Weak metal-metal transition in the vanadium oxytelluride Rb_{1-δ}V₂Te₂O, *Phys. Rev. B* 2018, 97, 214517.
- [3] Fogler, M. M.; Teber, S. Shklovskii, B. I. Variable-range hopping in quasi-one-dimensional electron crystals, *Phys. Rev. B* 2004, 69, 035413.
- [4] Bao, J.-K.; Li, L.; Tang, Z.-T.; Liu, Y.; Li, Y.-K.; Bai, H.; Feng, C.-M.; Xu, Z.-A.; Cao, G.-H. Cluster spin-glass ground state in quasi-one-dimensional K₂Cr₃As₃. *Phys. Rev. B* 2015, 91, 180404.
- [5] Tang, Z.-T.; Bao, J.-K.; Liu, Y.; Bai, H.; Jiang, H.; Zhai, H.-F.; Feng, C.-M.; Xu, Z.-A.; Cao, G.-H. Synthesis, crystal structure and physical properties of quasi-one-dimensional ACr₃As₃(A = Rb, Cs). Sci. China Mater. 2015, 58, 543-549.
- [6] Sun, F.; Guo, Z.; Liu, N.; Wu, D.; Lin, J.; Cheng, E.; Ying, T.; Li, S.; Yuan, W. Cs_{0.9}Ni_{3.1}Se₃: A Ni-Based Quasi-One-Dimensional Conductor with Spin-Glass Behavior. *Inorg. Chem.* 2018, 57, 3798-3804.

[7] Lin, J.; Deng, J.; Guo, Z.; Cheng, E.; Sun, F.; Liu, N.; Wang, B.; Li, S.; Yuan, W. Structure and physical properties of Ni-based quasi-one-dimensional selenides Rb_{0.9}Ni_{3.1}Se₃ and K_{0.7}Ni_{3.1}Se₃. *J. Alloy Compd.* 2019, 793, 425-432.